Available online at www.sciencedirect.com

ScienceDirect

Geochimica et Cosmochimica Acta 332 (2022) 285–306

Geochimica et Cosmochimica Acta

www.elsevier.com/locate/gca

Titanite links rare-element (meta-)pegmatite mineralization to Caledonian metamorphism

Haoyang Zhou ("周浩阳") [a,*], Axel Müller [a,b], Lars Eivind Augland [c,d], Magnus Kristoffersen [d], Muriel Erambert [d]

[a] *Natural History Museum, University of Oslo, P.O. Box 1172, Blindern, Oslo 0318, Norway*
[b] *Natural History Museum, Cromwell Road, London SW7 5BD, UK*
[c] *Centre for Earth Evolution and Dynamics (CEED), University of Oslo, P.O. Box 1172, Blindern, Oslo 0318, Norway*
[d] *Department of Geosciences, University of Oslo, P.O. Box 1047, Blindern 0316, Oslo, Norway*

Received 17 January 2022; accepted in revised form 7 June 2022; Available online 20 June 2022

Abstract

The metamorphic reworking of mineralized pegmatites during orogenesis remains unclear, making the genesis and the tectonomagmatic significance of pegmatite mineralization obscure. This study demonstrates the multiple utilities of titanite geochemistry in establishing the Caledonian metamorphic evolution of the world's largest intra-plutonic Nb-Y-F pegmatites in the Paleoproterozoic host rocks in Tysfjord, Northern Norway. A combination of titanite-specific barometry, Zr-in-titanite thermobarometry, and titanite U-Pb geochronology yields peak metamorphism of ~12 kbar and 730–750 °C at ~410 Ma for the host rocks and the largest metamorphosed Paleoproterozoic pegmatite (*meta*-pegmatite) in the region.

In relation to published U-Pb ages of 410–400 Ma for other regional *meta*-pegmatites, interpreted as Caledonian overprinting here, we argue that the Paleoproterozoic pegmatite protoliths have undergone metamorphism analogous to the host rocks, which was caused by allochthonous nappe stacking late in the Caledonian collisional orogeny (~440–400 Ma). Published formation ages of ~400–380 Ma for the regional undeformed pegmatites are 10–30 Ma younger than the peak metamorphism, supporting an anatectic link to the Caledonian post-collisional extension. The Caledonian orogeny led to strong shearing of preexisting pegmatite bodies and resetting of trace elements and U-Pb isotopic systems of the constituent minerals via mineral re-crystallization, inheritance of Pb isotopic components, and element diffusion. This cautions against the interpretation of *meta*-pegmatite-derived ages and geochemical information in tectonomagmatic terranes without detailed textural investigation.

Keywords: Titanite; Caledonian metamorphism; Metamorphosed pegmatites; Thermo-barometry; U-Pb geochronology; Trace elements

1. INTRODUCTION

Rare-element pegmatites are of upsurging significance as sources of critical metals such as Li, Be, Nb, Ta, Zr, Hf, and rare-earth elements (REEs; e.g., Kesler et al., 2012; Linnen et al., 2012; Gysi and Williams-Jones, 2013; Kaeter et al., 2018, 2021), and industrial minerals like ceramic feldspar and high-purity quartz (quartz with contaminating elements < 50 ppm which is very rare in nature but crucial for the high- and green-tech manufacture industries such as

* Corresponding author.
E-mail addresses: haoyang.zhou@nhm.uio.no (H. Zhou), a.b.muller@nhm.uio.no (A. Müller), l.e.augland@geo.uio.no (L.E. Augland), magnus.kristoffersen@geo.uio.no (M. Kristoffersen), m.m.l.erambert@geo.uio.no (M. Erambert).

https://doi.org/10.1016/j.gca.2022.06.014
0016-7037/

semiconductor, photovoltaic, and quartz glass applications; Glover et al., 2012; Haus et al., 2012; London and Kontak, 2012; Müller et al., 2012, 2015). They have been known to generate either from residual melts derived from crystallizing granitic plutons (e.g., Černý, 1991a, 1991b; Černý and Ercit 2005; London, 2008) or from metamorphic anatexis during orogenesis (e.g., Simmons et al., 2016; Müller et al., 2017). Therefore, pegmatites are also of great significance to pinpoint tectonomagmatic events in orogenic cycles (e.g., Černý, 1991c; Martin and De Vito, 2005; Buick et al., 2008; Lupulescu et al., 2011; Grimmer et al., 2015).

However, preexisting pegmatites can be metamorphosed during orogenesis (referred to as *meta*-pegmatites). The current knowledge of metamorphic reworking on *meta*-pegmatites remains inadequate, although a few studies have attempted to establish metamorphic reactions (e.g., Franz and Morteani, 1984; Černý et al., 1992), magmatic-crystallization and metamorphic ages (e.g., Glodny et al., 1998; Thöni and Miller, 2004; Habler et al., 2007), and deformation behavior (e.g., Eberlei et al., 2014). For a better understanding of the mineralization processes and tectonomagmatic significance of pegmatites, two open key questions are: 1) how to constrain the metamorphic conditions of *meta*-pegmatites; and 2) how metamorphism may change trace element geochemistry and U-Pb isotopic systems of the constituent minerals. The first question has rarely been addressed (e.g., Piber et al., 2009), probably because conventional pseudosection modeling requires single bulk-rock composition. This is impossible because of the considerable compositional variations in (meta-) pegmatites.

The Tysfjord tectonic window in the Caledonian nappes in Northern Norway exposes the Paleoproterozoic granite suite from the Baltic crystalline basement that was metamorphosed into gneiss during the Caledonian orogeny (Bartley, 1982; Andresen and Tull, 1986; Romer et al., 1992; Corfu et al., 2014; Müller et al., 2022). The Tysfjord granitic gneiss contains the largest known intra-plutonic 'pegmatites' with Nb-Y-F (NYF) signature that produce the world's second purest quartz resources (Müller et al., 2022). These 'pegmatites' have two age groups: Paleoproterozoic and Caledonian. The former highly sheared and deformed pegmatites (*meta*-pegmatites) are the main targets for high-purity quartz mining (Husdal, 2008; Müller et al., 2022). The relationship of these (meta-)pegmatites to the Caledonian metamorphism remains obscure due to the indeterminate metamorphic history of the region and the *meta*-pegmatites.

Titanite, a widespread metamorphic mineral across a wide P-T range (Frost et al., 2001; Kohn, 2017), has proven a powerful thermobarometer (Zr-in-titanite; Hayden et al., 2008), barometer (TZARS: titanite-zoisite/clinozoisite-anorthite-rutile-SiO_2; Kapp et al., 2009), geochemical indicator (e.g, Garber et al., 2017; Scibiorski et al., 2019), and petrochronometer (e.g., Essex and Gromet, 2000; Kohn, 2017). The combination of these benefits assigns a unique role to titanite in obtaining integrated pressure–temperature-timing (P-T-t) and geochemical information for metamorphism (e.g., Storey et al., 2007; Kohn and Corrie, 2011; Walters and Kohn, 2017; Zhang et al., 2018; Gordon et al., 2021; Soret et al., 2021).

In this contribution, we describe the titanite-bearing metamorphic assemblages for the regional granitic gneiss and the largest *meta*-pegmatite in Tysfjord. Metamorphic evolution is established by titanite-relevant thermobarometry and geochronology for the granitic gneiss and the *meta*-pegmatite. Integrating the published ages on these (meta-)pegmatites, we discuss 1) the roles of the Caledonian orogeny in the rare-element (meta-)pegmatite mineralization in the region and 2) how the Caledonian metamorphism changed the compositions and U/Pb isotopic systems of the pegmatite minerals.

2. GEOLOGICAL BACKGROUND

2.1. Paleoproterozoic magmatism and Caledonides in Tysfjord

The Baltic Shield is made up of an Archean core and a set of accreted terranes that comprise the Paleoproterozoic Svecofennian and the Neoproterozoic Sveconorwegian domains (Fig. 1A). The Trans-Scandinavian Igneous Belts (TIBs), emplacing along the southern and western margin of the Svecofennian domain, are considered arc magmatism formed in two periods (TIB-1: 1.85–1.76 Ga; TIB-2: 1.72–1.65 Ga; Högdahl et al. 2004). The closure of the Iapetus Ocean between Laurentia and Baltica led to several accretionary events throughout much of the Ordovician and into the early Silurian (e.g., Pedersen et al., 1992; Barnes et al., 2007; Augland et al 2012a, 2012b; see also Corfu et al., 2014 and references therein), before the final continental collision between the two continents commenced in the Llandovery (at least by ~437 Ma; e.g., Warvik et al., 2022). The collisional phase, the Scandian orogeny, resulted in the stacking of several far-traveled nappes (allochthons) onto western Baltica (Gee et al., 2008; Corfu et al., 2014). These Scandinavian Caledonian allochthons have traditionally been divided into four main tectonostratigraphic levels, Lower, Middle, Upper, and Uppermost based on their provenance, where the Lower and Middle Allochthons are derived from Baltica, the Upper Allochthon is derived from the Iapetus Ocean (including different island arcs and microcontinent terranes), and the Uppermost Allochthon is derived from Laurentia (Gee and Sturt, 1985; Gee et al., 2008). This simplified view on the tectonostratigraphy has been criticized (e.g., Corfu et al., 2014) but remains in use as a rough tectonostratigraphic framework.

The Tysfjord region, covering an area of about 4000 km^2 mainly in Hamarøy, Nordland, Northern Norway, is a tectonic window in the central Scandinavian Caledonides (Fig. 1B). The Tysfjord window is mostly bounded by the Uppermost Allochthon to the south and north, and the Upper Allochthon to the east. The Baltic crystalline basement is exposed in the tectonic window, which is predominately made up of TIB granites (Romer et al., 1992), with minor volcanic and sedimentary Svecofennian supracrustal rocks in the north and northwest (2.50–2.10 Ga and 1.91–1.88 Ga; Karlsen, 2000). It is worth pointing out that the Baltic basement exposed in Tysfjord can be

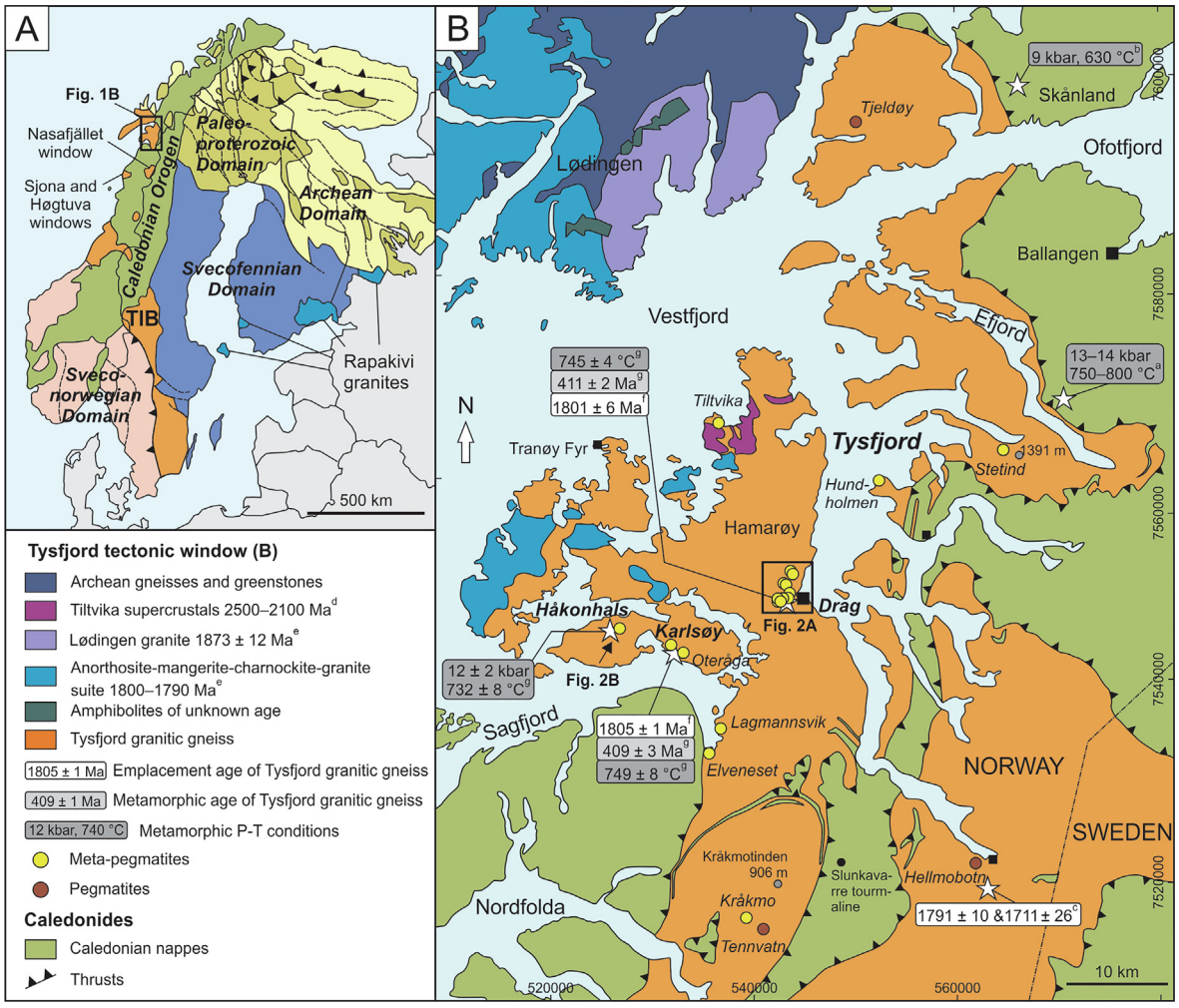

Fig. 1. A: Main terranes in Scandinavia (after Bergh et al., 2014). B: Schematic geologic map of the Tysfjord tectonic window (after Müller et al., 2022). The white stars mark sample locations of the reported ages and metamorphic conditions. Data sources: a–Hodges and Royden (1984); b–Steltenpohl and Bartley (1987); c–Romer et al. (1992); d–Karlsen (2000); e–Corfu (2004); f– Müller et al. (2022); g–this study.

allochthonous as part of the Lower Allochthon (see Hossack and Cooper, 1986; Gee et al., 2010; Gee and Stephens, 2020 and references therein). The emplacement of the granite in Tysfjord was dated to 1.80–1.79 Ga in Drag, Karlsøy, Hellmobotn (corresponding to TIB-1); and ~1.71 Ga in Hellmobotn (TIB-2; Fig. 1B; Romer et al., 1992; Müller et al., 2022). The granitic basement and the Caledonian nappes were subsequently metamorphosed at greenschist to amphibolite facies due to the allochthonous nappe stacking during the Scandian orogeny, e.g., the Tysfjord granite was metamorphosed into gneiss.

2.2. Multi-generations of rare-element (meta-)pegmatites in Tysfjord

The Tysfjord granitic gneiss contains numerous rare-element 'pegmatites' that belong to the Nb-Y-F (NYF) type in the classification scheme of Černý (1991a). Pegmatite mining occurred for decades for ceramic feldspar (1906–1970's) and has been revived since 1996 because of their high-purity quartz resources of greater economic interest. The Tysfjord 'pegmatites' show similar mineralogy but contrast in body sizes and degree of deformation. They are mainly made up of K-feldspar, plagioclase, quartz, and biotite, with dominant accessory minerals of allanite-(Ce), columbite-(Fe), gadolinite-(Y), fergusonite-(Y), thalénite-(Y), Y-rich fluorite, beryl, and sulfides (Husdal, 2008; Müller et al., 2022). Based on U-Pb dating on columbite and zircon, they comprise two age groups: 1772–1755 Ma (Paleoproterozoic) for those extensively deformed (*meta*-pegmatites) and 400–380 Ma (Caledonian) for those lacking deformation (Müller et al., 2022).

The *meta*-pegmatites always have larger sizes (up to several hundred meters in length), which cluster at Drag village in central Tysfjord (represented by two large *meta*-pegmatites: Jennyhaugen and Nedre Øyvollen; Fig. 2A) and also occur near the edge of the tectonic window (represented by the Håkonhals *meta*-pegmatite; Fig. 1B). They were formed from pegmatitic melts fractionated from grani-

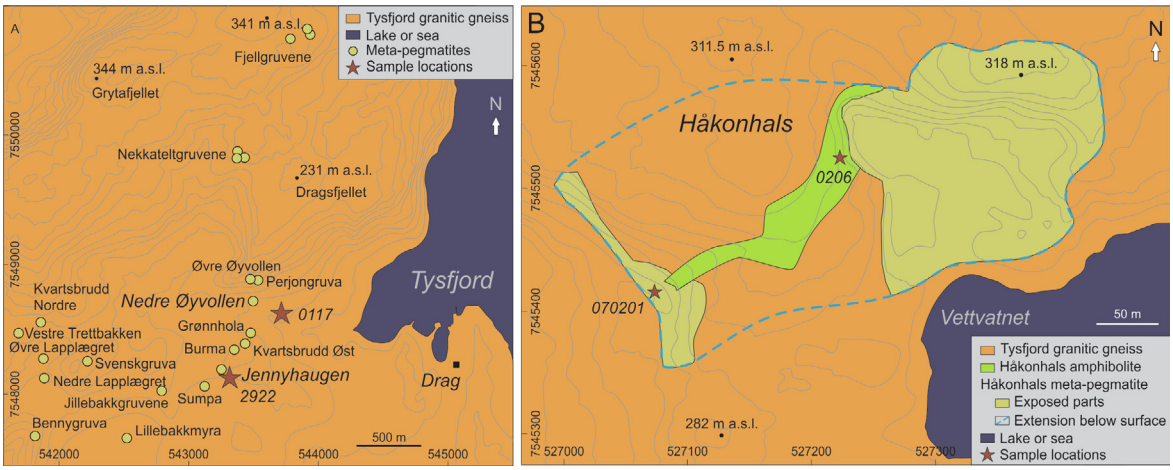

Fig. 2. Simplified geologic maps of the *meta*-pegmatite clusters at Drag (A) and the Håkonhals *meta*-pegmatite (B). Abbreviation: a.s.l. = above sea level.

tic magmatism (related to the Tysfjord granite) and subsequently underwent strong shearing and deformation during the Caledonian orogeny (Müller et al., 2022). Consequently, the primary mineralogical zonation of the pegmatites was destroyed to various degrees. Overall, they are made up of massive quartz cores surrounded by intermediate, blocky K-feldspar zones that evolve into foliated biotite-quartz-K-feldspar-plagioclase wall zones towards the margins of the bodies (Fig. 3A). The Caledonian pegmatites are much smaller (up to a dozen meters in length) and occur near the edge of the Tysfjord window (Fig. 1B). Being represented by Tennvatn, this type is undeformed and shows typical pegmatitic zonation. Notably, they are characterized by abundant amazonite (green variety of K-feldspar) and schorl. Anatectic melts from the Tysfjord granitic gneiss were proposed for their origin (Müller et al., 2022).

The lens-shaped Håkonhals *meta*-pegmatite is the largest one in Tysfjord (400-m long, 200-m wide, and 25-m thick; Fig. 2B). It is strongly deformed and in sharp contact with the mylonitized granitic gneiss. Interestingly, the upper part of the Håkonhals *meta*-pegmatite is in contact with an amphibolite body (~200-m long; hereinafter referred to as Håkonhals amphibolite; Figs. 2B and 3). The amphibolite shows fabrics parallel to the foliated wall of the *meta*-pegmatite and is locally rich in massive banded magnetite and fluorite. Similar amphibolite bodies have been observed in the granitic gneiss in road cuts at Finnøy and near Tømmerneset in southern Tysfjord.

3. SAMPLES AND ANALYTICAL METHODS

3.1. Sample information

Three samples of the Tysfjord granitic gneiss were taken from the central (Jennyhaugen and Nedre Øyvollen in Drag) and western (Karlsøy) Tysfjord tectonic window. Samples 2922 and 0117 are 61.5 m and 250 m from the Jennyhaugen and Nedre Øyvollen *meta*-pegmatites, respectively (Fig. 2A), while sample 3122 was taken from a road outcrop at Karlsøy (Fig. 1B). Samples 2922 and 3122 were reported to have zircon TIMS U-Pb ages of 1801 ± 6 Ma and 1805 ± 1 Ma (2σ), respectively, which point to the protolith of TIB-1 granite (Müller et al.,

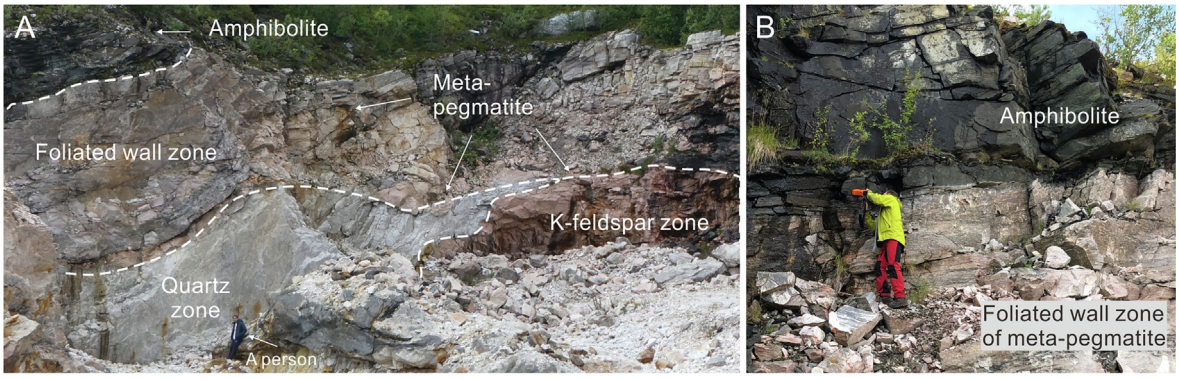

Fig. 3. Field photographs of the Håkonhals *meta*-pegmatite and overlying Håkonhals amphibolite. A: Meta-pegmatite body made up of massive quartz and K-feldspar zones surrounded by foliated biotite-quartz-K-feldspar-plagioclase wall zone. B: Foliated wall zone of *meta*-pegmatite in sharp contact with amphibolite.

2022). A *meta*-pegmatite sample containing rutile-titanite assemblage (070201) was taken from the blocky K-feldspar zone in Håkonhals, while an amphibolite sample (0206) was taken from the Håkonhals amphibolite (Fig. 2B). Bulk-rock major and trace element contents of these samples are provided in the supplementary text.

3.2. Electron Microprobe analysis of minerals

Mineral compositions of hornblende, biotite, plagioclase, titanite, epidote-group minerals, rutile, and garnet were measured in carbon-coated thin sections using a Cameca SX100 electron microprobe analyzer (EMPA) with five wavelength dispersive spectrometers at the Department of Geoscience, University of Oslo. An accelerating voltage of 15 kV, a beam current of 15nA, and a focused electron beam were used for all minerals, except for plagioclase (beam size of 5 μm). Matrix corrections were done according to the PAP procedure (Pouchou and Pichoir, 1991). Calibration standards, X-ray lines used, and counting time information are provided in a supplementary spreadsheet (Table S1).

3.3. LA-ICP-MS trace element analysis of titanite and rutile

Trace element contents of titanite and rutile were analyzed in thin sections using a Bruker Aurora Elite inductively coupled plasma-mass spectrometer (ICP-MS) connected to a Cetac LSX-213 G2 + laser (LA) at the Department of Geoscience, University of Oslo. The laser beam diameter was set at 40 μm for titanite and rutile-I, and 30 μm for rutile-II. A repetition rate of 10 Hz was set for the laser. Each analysis comprised 10-s background and 40-s data acquisition. Measured elements were Al, Si, P, Ca, Sc, Ti, V, Cr, Mn, Fe, Sr, Y, Zr, Nb, Sn, La, Ce, Pr, Nd, Sm, Eu, Gd, Tb, Dy, Ho, Er, Tm, Yb, Lu, Hf, Ta, W, Pb, Th, and U. Element concentrations, instrumental time-dependent drift, and mass discrimination were calibrated 1) against NIST 610, using SiO_2 contents measured by EMPA as internal standards for titanite (BCR-2G as a secondary standard to monitor the analytical accuracy), and 2) against BCR-2G, using TiO_2 contents for rutile (NIST 610 as a secondary standard). Each 12–15 analyses of unknown titanite/rutile were bracketed by 3 analyses of NIST 610 and BCR-2G. Data reduction and calibration were done via the software Glitter.

3.4. ID-TIMS U-Pb dating of titanite

Titanite was separated from the two Tysfjord granitic gneiss samples (2922 and 3122) and the Håkonhals amphibolite sample (0206), applying the conventional protocol of crushing followed by the hydro-, magnetic, and heavy-liquid separation methods. Pure crystals were further hand-picked under a binocular microscope. The U-Pb dating on titanite was carried out by isotope dilution-thermal ionization mass spectrometry (ID-TIMS) at the Department of Geoscience, University of Oslo. The selected titanite grains were air abraded (Krogh, 1982) and repeatedly washed in dilute HNO_3, prior to the addition of an in-house ^{202}Pb-^{205}Pb-^{235}U tracer that has recently been calibrated to the EARTHTIME (ET) 100 Ma solution (Ballo et al., 2019). The grains were then dissolved on a hot plate in HF (+ HNO_3) at ca. 140 °C for > 5 days. After dissolution, the titanite samples were purified with a single-stage HBr-HCl column chemistry procedure. The purified solutions were loaded on zone refined Re filaments and measured on a Finnigan MAT262 TIMS (for further analytical details, see Augland et al., 2010; Ballo et al., 2019). The raw data were reduced using Tripoli (Bowring et al., 2011). Analytical errors and corrections were incorporated and propagated using an Excel macro based on published algorithms (Schmitz and Schoene, 2007). All U-Pb data were plotted using Isoplot (Ludwig, 2003) using the decay constants of Jaffey et al. (1971). Common Pb correction was performed using the Stacey and Kramers (1975) Pb evolution model at 1.8 Ga (the protolith age of the Tysfjord granitic gneiss), with Pb blank generally < 1.5 pg with a composition of $^{206}Pb/^{204}Pb = 18.04 \pm 0.40$, $^{207}Pb/^{204}Pb = 15.22 \pm 0.30$, and $^{208}Pb/^{204}Pb = 36.67 \pm 0.50$.

3.5. LA-ICP-MS U-Pb dating of titanite

In-situ U-Pb dating of titanite from the Håkonhals amphibolite (0206) and *meta*-pegmatite (070201) was run on thin sections using the aforementioned LA-ICP-MS (REE and Y were measured simultaneously applying NIST 610 as an external standard). A beam diameter of 40 μm and a repetition rate of 10 Hz were set for the laser. Each analysis consisted of 10-s background and 40-s data acquisition. Titanite OLT1 (Kennedy et al., 2010) was applied as the external standard to calibrate the U-Pb isotope fractionation, and titanite Arkaroola (Elburg et al., 2003) was used as unknown to evaluate analytical accuracy. Every 18–20 analyses of unknown titanite were bracketed by 3 analyses of OLT1 (and NIST 610). Data reduction and calibration, comprising background subtraction and correction for mass discrimination, laser-induced U–Pb downhole fractionation and time-dependent instrumental drift, were done via an in-house spreadsheet that was described by Andersen et al. (2009). The analyses yielded weighted mean $^{206}Pb/^{238}U$ ages of 1018 ± 9 Ma (2σ, n = 14) for OCL1 and 448 ± 17 Ma (2σ, n = 3) for Arkaroola, which are in good agreement with their reported TIMS concordia ages of 1014.8 ± 2.0 Ma (Kennedy et al., 2010) and 439 ± 1 Ma (Elburg et al., 2003), respectively. All U-Pb data are uncorrected for common Pb and are plotted using Isoplot (Ludwig, 2003).

4. RESULTS

4.1. Petrography and mineral chemistry

4.1.1. The Tysfjord granitic gneiss

The Tysfjord granitic gneiss is mainly made up of hornblende, biotite, plagioclase, K-feldspar, and quartz, with titanite, epidote-group minerals, fluorapatite, zircon, pyrite, and magnetite being accessory components. The alignment of biotite together with hornblende defines the foliation. The granitic gneiss at Drag is slightly different from the

one at Karlsøy in terms of color and modal mineralogy (Fig. 4A–4C). At Drag, it is gray-whitish, made up of hornblende (5–10%; volume percent), biotite (15–20%), plagioclase (30–35%), K-feldspar (20–25%), and quartz (20–25%). At Karlsøy, it is light-pinkish and the modal mineralogy is similar except for equal proportions (25–30%) of plagioclase and K-feldspar. Garnet (almandine-grossular; coexisting with titanite and epidote-group minerals) occurs as a common accessory component in the granitic gneiss at Drag but has not been identified at Karlsøy. All mineral textures are shown in Figs. 5–7. The mineral chemistry is listed in Table S1 and plotted in Fig. 8. They are reported below to highlight the similarities and contrasts at Drag and Karlsøy.

Hornblende (0.5 to several mm; hastingsite and ferropargasite; Table S1) coexists with titanite and contains mineral inclusions of titanite and epidote-group minerals (Fig. 5A and 5B). Hornblende at Drag has lower Mg# [Mg/(Mg + Fe^{2+}) × 100] but higher TiO_2 contents than that at Karlsøy (Fig. 8A).

At Drag, biotite displays dark (core) and bright (rim) domains on backscattered electron (BSE) images, with dark domains texturally in equilibrium with titanite (Fig. 6A). The dark and bright domains have identical Mg#, F and Cl contents but are distinct in X_{Na} [Na/(Na + K + Ca): 0.06 ± 0.02 vs. 0.01 ± 0.01; Fig. 8B]. At Karlsøy, biotite is homogenous and has higher Mg#, F but lower Cl contents, with low X_{Na} (~0.01) comparable to the bright biotite at Drag.

Plagioclase (0.2–1 mm) shows a bright core and a dark rim on BSE images (Fig. 6B–6D). The core coexists with titanite and hornblende, while the rim is intergrown with low X_{Na} biotite and Ba-bearing K-feldspar. The An number (anorthite mol%) is higher in the core than the rim (An_8 vs. An_3 at Drag, and An_5 vs. An_3 at Karlsøy).

Epidote-group minerals are present as 1) coarse, prismatic grains coexisting with hornblende and titanite (50–200 μm; Fig. 5A and 5B), and 2) small inclusions encapsulated in titanite and hornblende (5–20 μm; Fig. 7A and 7B). They are made up of core, mantle, and rim showing decreasing BSE brightness (Fig. 7C–7F) and comprise (ferri-)allanite, LREE-rich epidote, and epidote (Fig. 8C). Notably, the sharp contact of the mantle of the epidote-group minerals with titanite and hornblende points to equilibrium among them. Epidote-group minerals have considerable total light REE contents (ΣLREE: La, Ce, Pr, and Nd): extremely high throughout the whole grain at Drag (11–19 wt%) and in the grain core-mantle at Karlsøy (9–16 wt%).

Likewise, titanite has two occurrences: 1) as coarse euhedral grains (rhombic; optically light yellow; 50–500 μm) in aggregates coexisting with hornblende, epidote-group minerals, and fluorapatite (Figs. 5A, 5B, 6A, and 7D); and 2) as tiny, oriented inclusions together with epidote-group minerals enclosed in hornblende (Figs. 5A, 7A, and 7B). It displays sector and patchy zoning on BSE images (Fig. 6A). The titanite at Drag shows slightly lower X_{Ti} [Ti/(Al + Fe + Ti)] and higher F content than that at Karlsøy (X_{Ti} = 0.79 ± 0.02 vs. 0.83 ± 0.02; Fig. 8D).

4.1.2. The Håkonhals amphibolite

The Håkonhals amphibolite (Fig. 5C) is composed of hornblende (35%), biotite (30%), plagioclase (15%), quartz (10%), titanite (3%), epidote (2%), magnetite (3%),

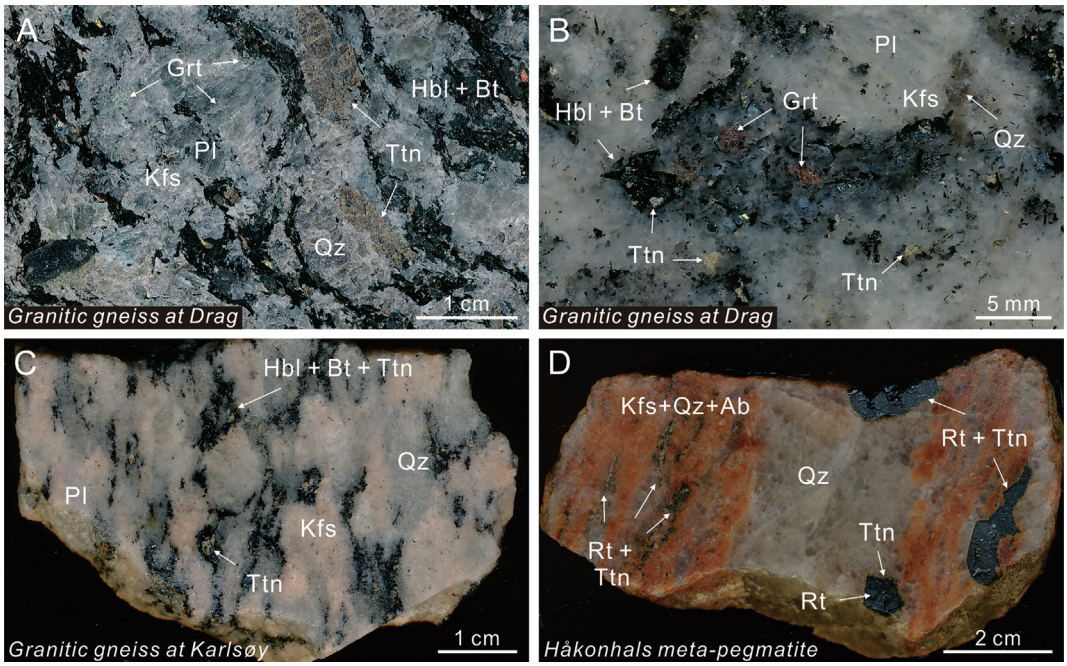

Fig. 4. A and B: Gray-whitish Tysfjord granitic gneiss at Drag made up of hornblende (Hbl), biotite (Bt), plagioclase (Pl), K-feldspar (Kfs), quartz (Qz), together with garnet (Grt) and coarse-grained titanite (Ttn). C: Light-pinkish, titanite-bearing and garnet-free Tysfjord granitic gneiss at Karlsøy. D: Rutile-titanite assemblage from the Håkonhals *meta*-pegmatite. Coarse-grained rutile (Rt) surrounded by fine-grained titanite occurs in the foliated matrix made up of quartz, K-feldspar, and subordinate albite (Ab).

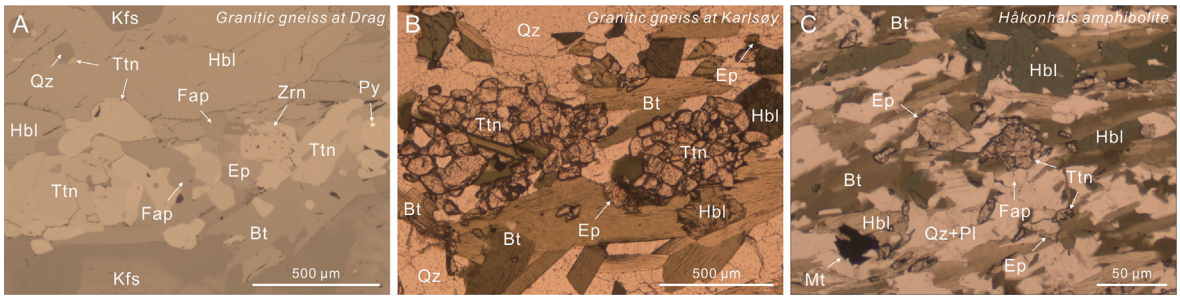

Fig. 5. Optical microscope images of the Tysfjord granitic gneiss and the Håkonhals amphibolite. A: Titanite (Ttn) aggregates coexisting with quartz (Qz), epidote-group minerals (Ep), fluorapatite (Fap), hornblende (Hbl), pyrite (Py), and inherited coarse-grained zircon (Zrn) under reflected light. Titanite also occurs as mineral inclusions in hornblende. B: Titanite aggregates and epidote-group minerals in the assemblage of hornblende and biotite (Bt) under plane-polarized light. C: Titanite as discrete grains under plane-polarized light, showing orientation parallel to the foliation that is defined by hornblende and biotite. Other abbreviations: Kfs = K-feldspar, Mt = magnetite.

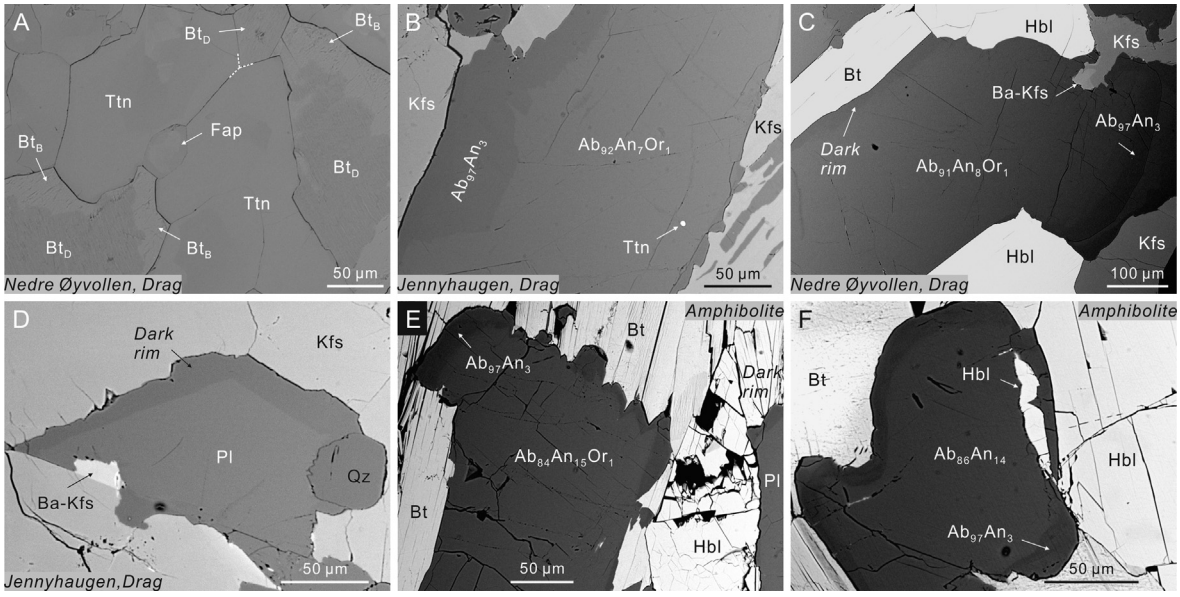

Fig. 6. Backscattered electron (BSE) images of the Tysfjord granitic gneiss (A–D) and the Håkonhals amphibolite (E–F). A: Zoned biotite comprising dark (Bt_D; high X_{Na}) and bright (Bt_B; low X_{Na}) domains. Titanite (Ttn) shows patchy zoning and is in equilibrium with dark biotite. B: Zoning plagioclase (Pl) comprising bright core and dark rim. There is titanite in the bright core of plagioclase. C and D: Dark rim of plagioclase coexisting with biotite, Ba-rich K-feldspar (Ba-Kfs), and quartz (Qz). The bright plagioclase core coexists with hornblende (Hbl). E: Plagioclase showing dark rim surrounded by biotite. F: Hornblende is in sharp contact with the bright plagioclase core. Other abbreviations: Ab = albite, An = anorthite, Or = orthoclase.

pyrite + chalcopyrite (2% combined), and fluorapatite + zircon (<1%). The mineral chemistry is listed in Table S1 and reported below.

Hornblende (0.2–2 mm; hastingsite; Table S1) shows Mg# higher than that of the granitic gneiss and TiO_2 content identical to that at Karlsøy (Fig. 8A).

Biotite is homogeneous (0.2–1 mm) and shows higher Mg# in comparison to that from the granitic gneiss (Fig. 8B). Its X_{Na} (~0.01) is comparable to the bright biotite (low X_{Na}) in the granitic gneiss.

Plagioclase (30–200 μm), likewise, displays a bright core and a thin rim (An_{15} vs. An_4; Fig. 6E and 6F).

Epidote is present as euhedral, prismatic grains (100–500 μm; Fig. 5C) and also shows core-mantle-rim zonation of decreasing BSE brightness (Fig. 7G). The epidote rim is in sharp contact with titanite and hornblende, implying equilibrium among them. ΣLREE is only rich in the grain core and mantle (3–10 wt%; Fig. 8C).

Titanite occurs as wedge-shaped discrete grains (50–300 μm; Fig. 5C) with the long axis parallel to the foliation. Except for a few grains with irregular cores that are optically darker yellow and bright under the BSE (type 1; Fig. 7H), all observed grains are optically light yellow and quite homogenous under the BSE (Fig. 7G) and can be sub-grouped as types 2 and 3 based on their REE patterns (see next section). Some titanite grains contain inclusions of titanomagnetite and ilmenite intergrowth (Fig. 7I). Types 2 and 3 titanite have identical X_{Ti} (0.91 ± 0.01), which is slightly higher than type 1 (X_{Ti} = 0.88 ± 0.02; Fig. 8D).

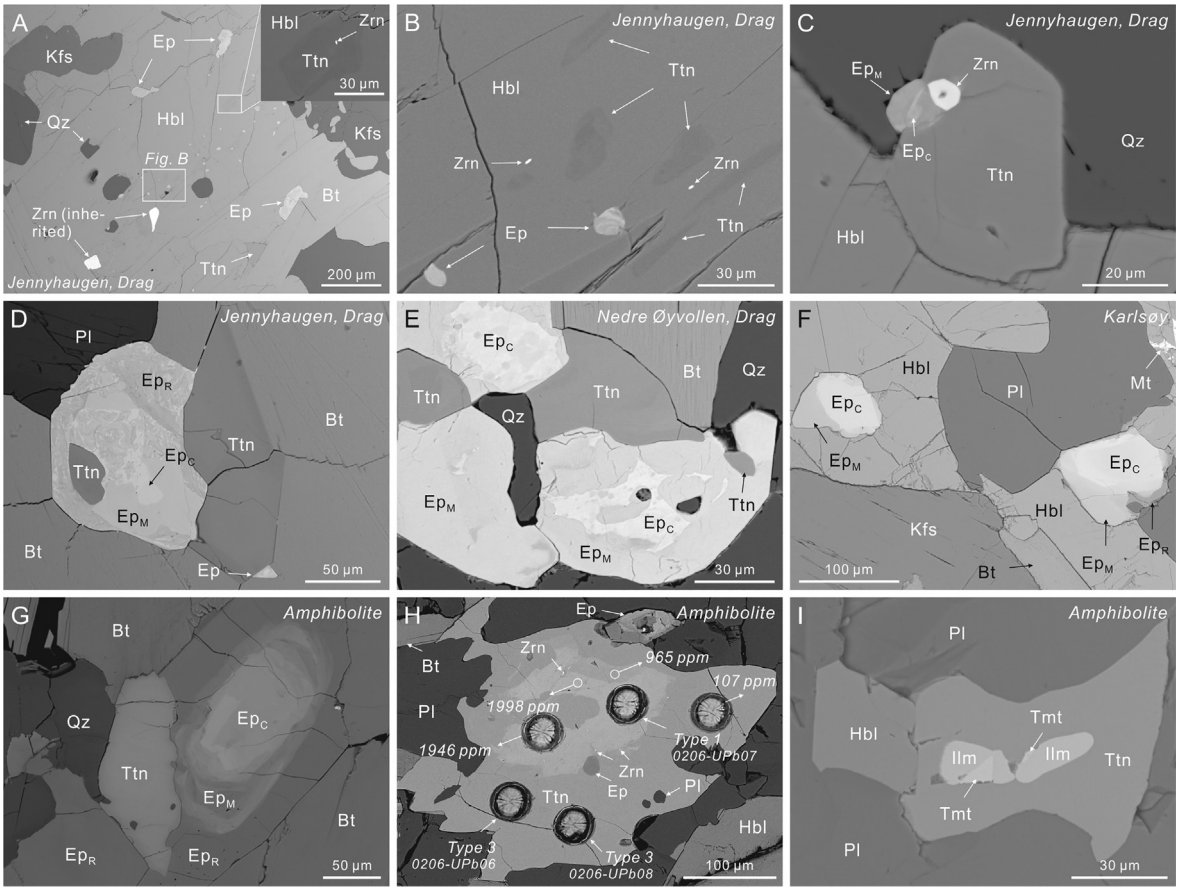

Fig. 7. BSE images showing occurrences of titanite (Ttn) and zoned epidote-group minerals (Ep; made up of core-C, mantle-M, and rim-R) in the Tysfjord granitic gneiss (A–F) and the Håkonhals amphibolite (G–I). A and B: Titanite and epidote-group minerals both as coarse grains and oriented tiny inclusions together with quartz (Qz) in hornblende (Hbl). There are two types of zircon (Zrn): coarse grains of inherited origin and tiny grains of metamorphic origin. C: Euhedral titanite coexisting with zircon and zoned epidote-group minerals. D: Zoned epidote-group mineral, with its rim altered and its mantle in sharp contact with titanite. E: Titanite coexisting with mantle of the epidote-group minerals. F: Euhedral zoned epidote-group minerals encapsulated by hornblende. G: Titanite intergrown with dark epidote rim. H: Titanite made up of bright (type 1) and dark (type 3) domains, with zircon inclusions in between while epidote and plagioclase (Pl) inclusions in the dark domains. U/Pb isotopic ratios of the three labeled laser points are plotted in Fig. 13A. The numbers are Zr contents and the white circles mark corresponding locations of EMPA analyses. I: Titanite showing inclusions of relict assemblages of titanomagnetite (Tmt) and ilmenite (Ilm). Other abbreviations: Bt = biotite, Kfs = K-feldspar.

4.1.3. The rutile-titanite assemblage from the Håkonhals meta-pegmatite

The rutile-titanite assemblage from the Håkonhals *meta*-pegmatite is present as porphyroblasts (up to several cm) in the matrix of quartz, K-feldspar, and subordinate albite (Fig. 4D). It shows elongation parallel to the foliation defined by ribbon-like K-feldspar. Rutile can be divided into two generations: rutile-I and -II. Rutile-I, present as coarse cores (>several mm), is rimmed by rutile-II (euhedral to subhedral; 20–80 μm) together with titanite and quartz (Fig. 9A). The mineral chemistry is listed in Table S1.

Rutile-I can be termed as niobian rutile or ilmenorutile given its high Nb and Fe (see below). It has three populations of mineral inclusions: 1) droplet-like polycrase with variable Y and U [$(Y,U)(Ti,Nb,Fe)_2O_6$; referred to as polycrase-I; Fig. 9A and 9B], 2) fluorite + K-feldspar + albite (Fig. 9C), and 3) ilmenite/titanite + columbite-(Fe) + zircon + cassiterite + scheelite + wolframite (Fig. 9D). Populations 1 and 2 are randomly distributed in rutile-I, interpreted as primary inclusions. Population 3, as ribbon-like conjugate trails, shows orientation parallel with strain-induced fabrics.

Rutile-II is darker and sometimes shows irregular, subtle zonation under the BSE. It coexists with a Ca-rich variant of polycrase [$(U,Ca,Y)(Ti,Nb)_2O_6$; referred to as polycrase-II; Fig. 9B]. Columbite-(Fe) of irregular shape is distributed along the contact of rutile-I and -II (Fig. 9E). Both rutile-II and polycrase-II are surrounded by radiated aggregates of chlorite, being accompanied by the replacement of polycrase-II into unrecognized Ti, Nb-rich phases with variable Si, Ca, U, Y of radiated morphology [referred to as Si-(Ca,Y,U)(Ti,Nb)-O; Fig. 9B, 9E, and 9I]. EMPA analyses show that rutile-I has much higher chemical impurity than rutile-II: Nb_2O_5 = 16.4–20.6 vs. 1.3–5.0 wt%, FeO = 7.7–10.1 vs. 0.2–1.2 wt%, Ta_2O_5 = 1.1–1.8 vs. 0.3–1.1 wt% (Fig. 10A).

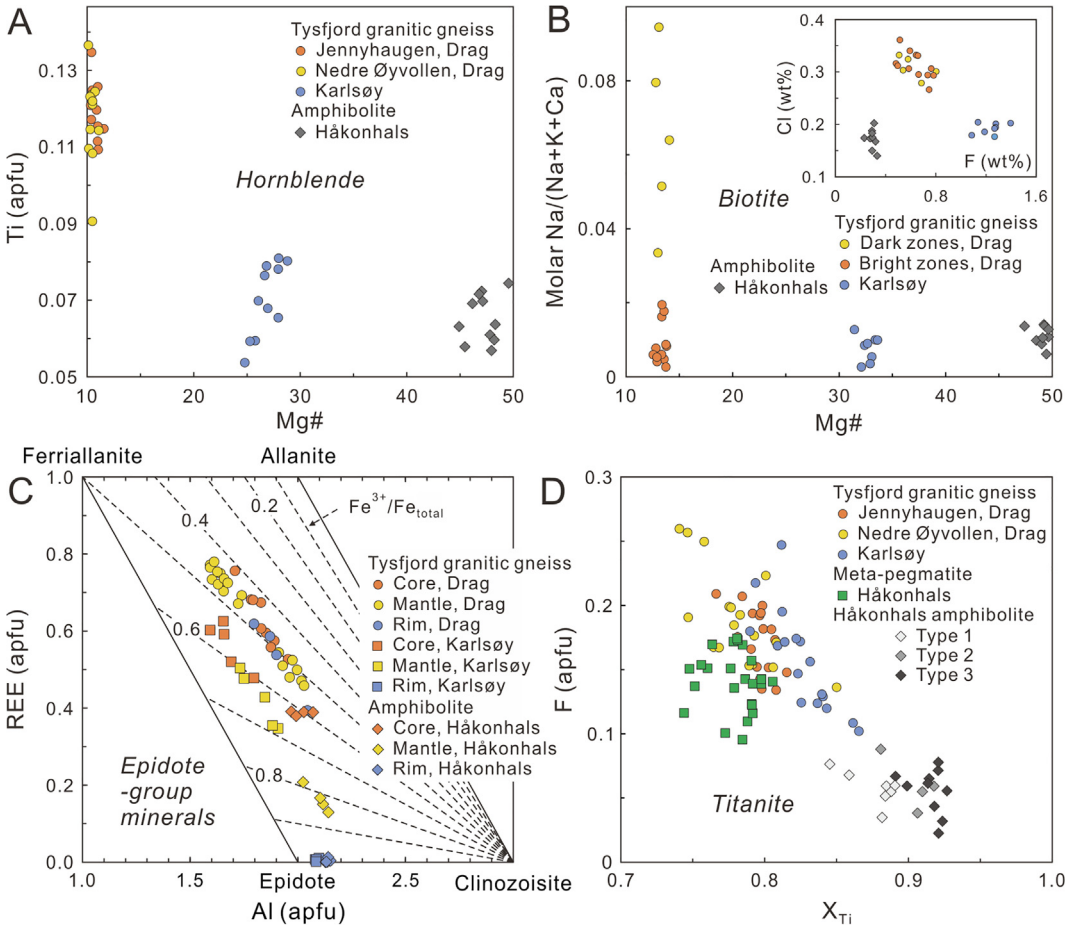

Fig. 8. Binary plots of mineral composition for the Tysfjord granitic gneiss at Drag (Jennyhaugen and Nedre Øyvollen) and Karlsøy, the Håkonhals amphibolite, and the Håkonhals *meta*-pegmatite. A: Hornblende. B: Biotite (dark and bright domains for Drag and unzoned biotite for other samples). C: Zoned epidote-group minerals (core, mantle, and rim; the dotted lines are from Petrík et al., 1995). D: Titanite.

Titanite (50–500 μm) is intergrown with rutile-II (Fig. 9F) and contains relicts of rutile-I (Fig. 9G). Zircon is found intergrown with titanite (Fig. 9G and 9H) and along the contact of titanite and rutile-I (Fig. 9F). The titanite shows X_{Ti} of 0.78 ± 0.01 similar to that in the granitic gneiss (Fig. 8D). It also has high Y_2O_3, Nb_2O_5, and SnO contents (1.1 ± 0.3, 0.9 ± 0.3, and 0.2 ± 0.1 wt%, respectively).

4.2. Trace element geochemistry of titanite and rutile

All trace element data of titanite and rutile from the Tysfjord granitic gneiss and the Håkonhals amphibolite and *meta*-pegmatite are listed in Table S2. For comparison, bulk-rock REE patterns of the granitic gneiss and the amphibolite are shown in Fig. 11A.

4.2.1. Trace element geochemistry of titanite

Titanite in the granitic gneiss at Drag has 3439 ± 962 ppm ΣREE (total REEs), 3189 ± 950 ppm Y, 69 ± 38 ppm U, 4 ± 2 ppm Th, and 79 ± 23 ppm Zr. It shows depleted LREE and fractionated (flat to depleted) HREE, with weak positive Ce and negative Eu anomalies: $Ce/Ce^* = Ce_N/(La_N \times Pr_N)^{0.5}$ = 1.0–1.2, $Eu/Eu^* = Eu_N/(Sm_N \times Gd_N)^{0.5}$ = 0.4–0.7 (subscript N denotes chondrite-normalized values; Fig. 11B).

Titanite in the granitic gneiss at Karlsøy has similar ΣREE, Y, U, Th, and Zr contents: 4723 ± 836, 3634 ± 409, 34 ± 20, 8 ± 5, and 83 ± 17 ppm, respectively. It also shows depleted LREE with negative Eu anomaly (Eu/Eu^* = 0.3) but consistently flat HREE (Fig. 11C). All analyses yield weak positive Ce anomalies (Ce/Ce^* = 1.2), except for three analyses with strong negative Ce anomalies (Ce/Ce^* = 0.04–0.3).

Titanite in the amphibolite can be texturally and geochemically categorized into three types showing decreasing contents in Zr, Y, Nb, ΣREE, Pb, Th, and U (Fig. 10C). They all have negligible Ce anomalies but are distinguishable from Eu anomalies as well as LREE fractionation degree. The latter is measured by $(Sm/La)_N$ values: a value below 1 suggests LREE enrichment. Type 1 (the bright cores of the titanite; Fig. 7H) has extraordinarily high Zr (1782 ± 340 ppm), $(Sm/La)_N < 1$, and $Eu/Eu^* = 0.2$. Type 2 has $(Sm/La)_N = 2.8 \pm 1.3$ and $Eu/Eu^* = 1.3 \pm 0.5$. Type 3 (U = 14 ± 13 ppm, Th = 2 ± 1 ppm, Zr = 59 ± 9 ppm) has $(Sm/La)_N = 11.2 \pm 4.9$ and $Eu/Eu^* = 1.0 \pm 0.1$, show-

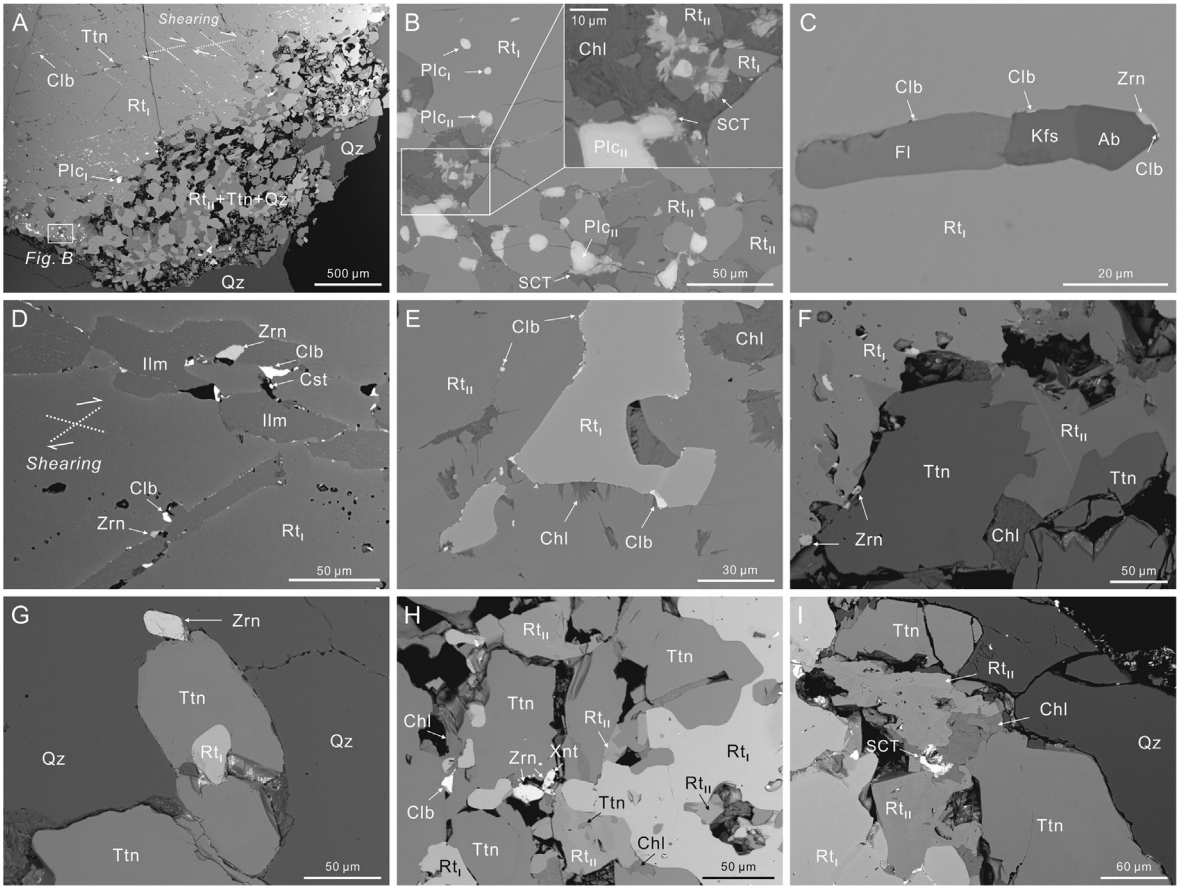

Fig. 9. BSE images of the rutile-titanite assemblage from the Håkonhals *meta*-pegmatite. A: Rutile-I (Rt_I) rimmed by rutile-II (Rt_{II}), titanite (Ttn), and quartz (Qz). The white dotted lines mark the orientation of population 3 inclusions in rutile-I, indicating shearing-induced metamorphic reactions along the conjugate joints. B: Decomposition of rutile-I and population 1 inclusions of polycrase-I (Plc_I) into rutile-II (Rt_{II}) and polycrase-II (Plc_{II}). The latter is replaced by radiated-shaped chlorite (Chl) to form an unrecognized phase of Si-(Ca,Y,U)(Ti,Nb)-O (SCT). C: Population 2 inclusion in rutile-I made up of fluorite (Fl), K-feldspar (Kfs), and albite (Ab). D: A close-up of population 3 inclusions made up of ilmenite (Ilm), columbite-(Fe) (Clb), zircon (Zrn), and cassiterite (Cst). E: Distribution of tiny columbite-(Fe) along the contact of rutile-I and -II. F: Zircon present along the contact of rutile-I and titanite-rutile-II intergrowth. G: Titanite containing relict rutile-I and coexisting with zircon. H: Breakdown of rutile-I into titanite and rutile-II. Note that euhedral zircon is intergrown with xenotime (Xnt) and in contact with zoned rutile-II. I: Zoned rutile-II surrounded by chlorite.

ing REE patterns (Fig. 11D) analogous to the granitic gneiss titanite.

Titanite from the Håkonhals *meta*-pegmatite has the highest ΣREE and Y contents (8287 ± 2739 and 8248 ± 3203 ppm, respectively). It displays depleted LREE and enriched HREE (Fig. 11E), with negligible Ce and negative Eu anomalies (Ce/Ce* = 0.9–1.1, Eu/Eu* = 0.2). Uranium, Th, and Zr contents are 135 ± 82, 108 ± 41, and 51 ± 15 ppm, respectively.

4.2.2. Trace element geochemistry of rutile

The trace element data of rutile-I and -II from the Håkonhals *meta*-pegmatite are shown in Fig. 10A. Rutile-I has higher contents of high field strength elements (HFSEs, e.g., Zr, Hf, Nb, Ta, W, Sn, U) than rutile-II (Zr = 486 ± 87 vs. 66 ± 25 ppm). Niobium/Ta ratios are relatively constant in rutile-I but in a wide range in rutile-II (Fig. 10B). Yttrium, Th, and REE contents in rutile-I are near or below the detection limits (<0.01–1 ppm) and in rutile-II are 82 ± 52, 5 ± 4, and 142 ± 83 ppm, respectively. Rutile-II displays depleted LREE and enriched HREE, with slightly variable Ce and negative Eu anomalies (Ce/Ce* = 0.8–1.2, Eu/Eu* = 0.1–0.2; Fig. 11F), which is identical to the co-existing titanite (Fig. 11E).

4.3. U-Pb dates of titanite

4.3.1. U-Pb dates of titanite from the Tysfjord granitic gneiss

All ID-TIMS U-Pb data of titanite from the Tysfjord granitic gneiss are listed in Table 2 and plotted in Fig. 12A. For the granitic gneiss at Drag, all titanite analyses, except for analysis 610/s13, are concordant and overlap within errors, giving a concordia age of 410.6 ± 1.5 Ma (2σ; decay constant errors included; MSWD = 0.12). 610/s13 is reversely discordant and slightly younger than the remaining analyses, interpreted to reflect a combination of residual Pb-loss and uncorrected common Pb.

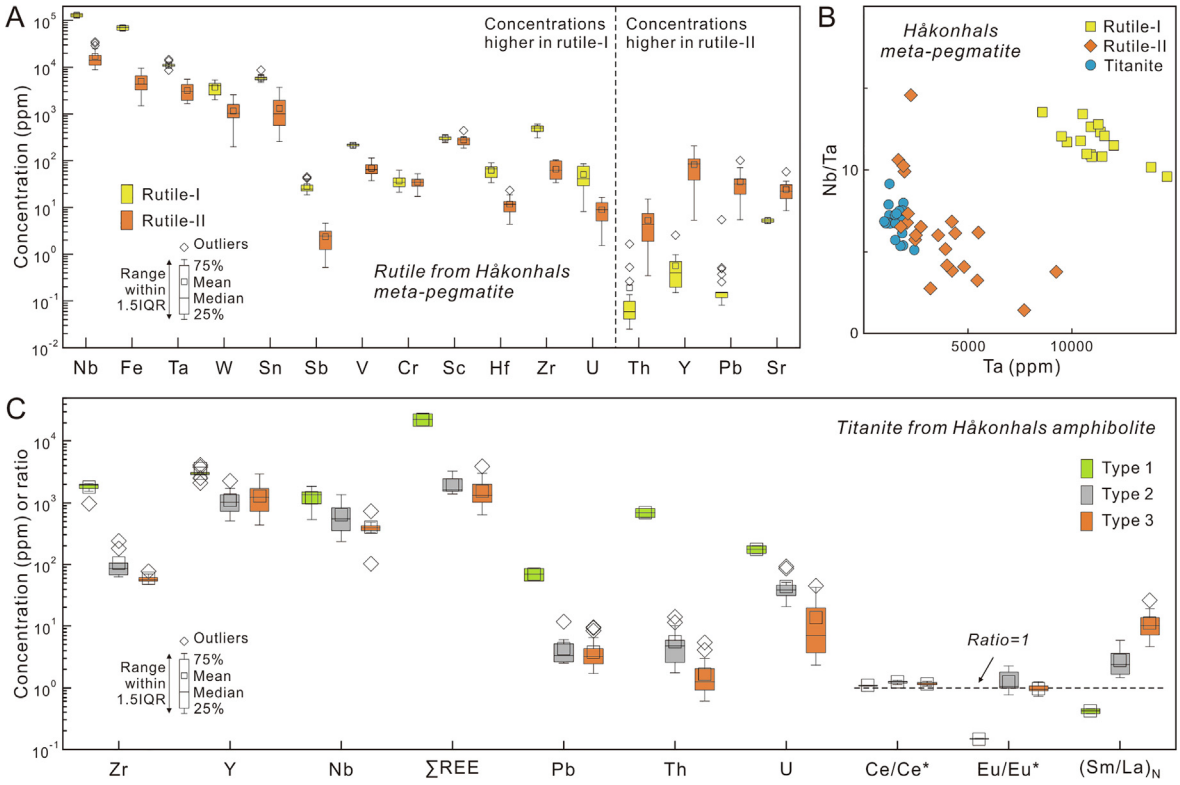

Fig. 10. A: Box chart showing element concentrations in rutile-I and -II from the Håkonhals *meta*-pegmatite (IQR = interquartile range; the first five box data on the left are from EMPA analyses that generally have higher precision for elements of high abundance, while the rest are LA-ICP-MS data; components below detection limits are plotted using their detection limits). B: Nb/Ta vs. Ta plot for rutile-I and -II and titanite from the Håkonhals *meta*-pegmatite. Note that EMPA data are shown for rutile-I, EMPA and LA-ICP-MS data for rutile-II, and LA-ICP-MS data for titanite. Scattered Nb/Ta ratios irrelevant with Ta for rutile-II suggest diffusive Nb/Ta fractionation. C: Box chart showing trace element concentrations and ratios of the three types of titanite from the Håkonhals amphibolite (LA-ICP-MS data). $(Sm/La)_N$: chondrite-normalized ratio, measuring the fractionation degree of LREE relative to MREE.

For the granitic gneiss at Karlsøy, all titanite analyses but analysis 610/s15 are concordant and overlap within errors, giving concordia age of 408.7 ± 2.9 Ma (2σ; decay constant errors included; MSWD = 0.07). The $^{206}Pb/^{238}U$ ages of the three concordant analyses are identical within uncertainties to 610/s15, giving a weighted average of 409.1 ± 3.4 Ma (2σ; MSWD = 2.7).

Combining all analyses except for 610/s13, a weighted average $^{206}Pb/^{238}U$-age of 409.6 ± 2.0 Ma (2σ; MSWD = 0.51) is obtained, which is interpreted to represent the best estimate of the crystallization of the titanite from the Tysfjord granitic gneiss.

4.3.2. U-Pb dates of titanite from the Håkonhals amphibolite

For the amphibolite, U-Pb isotopic ratios of titanite were measured by TIMS and LA-ICP-MS. For the TIMS analyses, all grains are discordant (Table 2; Fig. 12B), defining a regression line in a Wetherill diagram with an upper intercept age of 1736 ± 3 Ma and a lower intercept age of 409 ± 27 Ma (2σ; MSWD = 0.89). The LA-ICP-MS U-Pb data are related to the aforementioned three titanite types (Table S3; Fig. 13A). Type 1 analyses are the least discordant, roughly giving a Paleoproterozoic upper intercept age in a Wetherill diagram. Type 3 analyses are extremely discordant, defining a regression line in a Tera-Wasserburg plot with a lower intercept age of 413 ± 11 Ma (2σ; MSWD = 1.1; n = 28) and an initial $^{207}Pb/^{206}Pb$ ratio (Y-intercept) of 0.753 ± 0.012 (95% confidence). Type 2 analyses lie in the regression line defined by type 3 analyses.

4.3.3. U-Pb dates of titanite from the Håkonhals meta-pegmatite

For the titanite in the rutile-titanite assemblage from the Håkonhals *meta*-pegmatite, all LA-ICP-MS U-Pb data are shown in Table S3 and plotted in Fig. 13B. A regression through all data points give a lower intercept age of 409 ± 18 Ma (2σ; MSWD = 7.3; n = 36) and an initial $^{207}Pb/^{206}Pb$ ratio of 0.408 ± 0.045 (95% confidence).

5. DISCUSSION

5.1. P-T constraints on regional metamorphism

In the Tysfjord granitic gneiss, the long axes of titanite and epidote-group minerals parallel with the foliation and the coexistence of titanite and epidote-group minerals with hornblende (Fig. 7A–7F) indicate a peak metamorphic

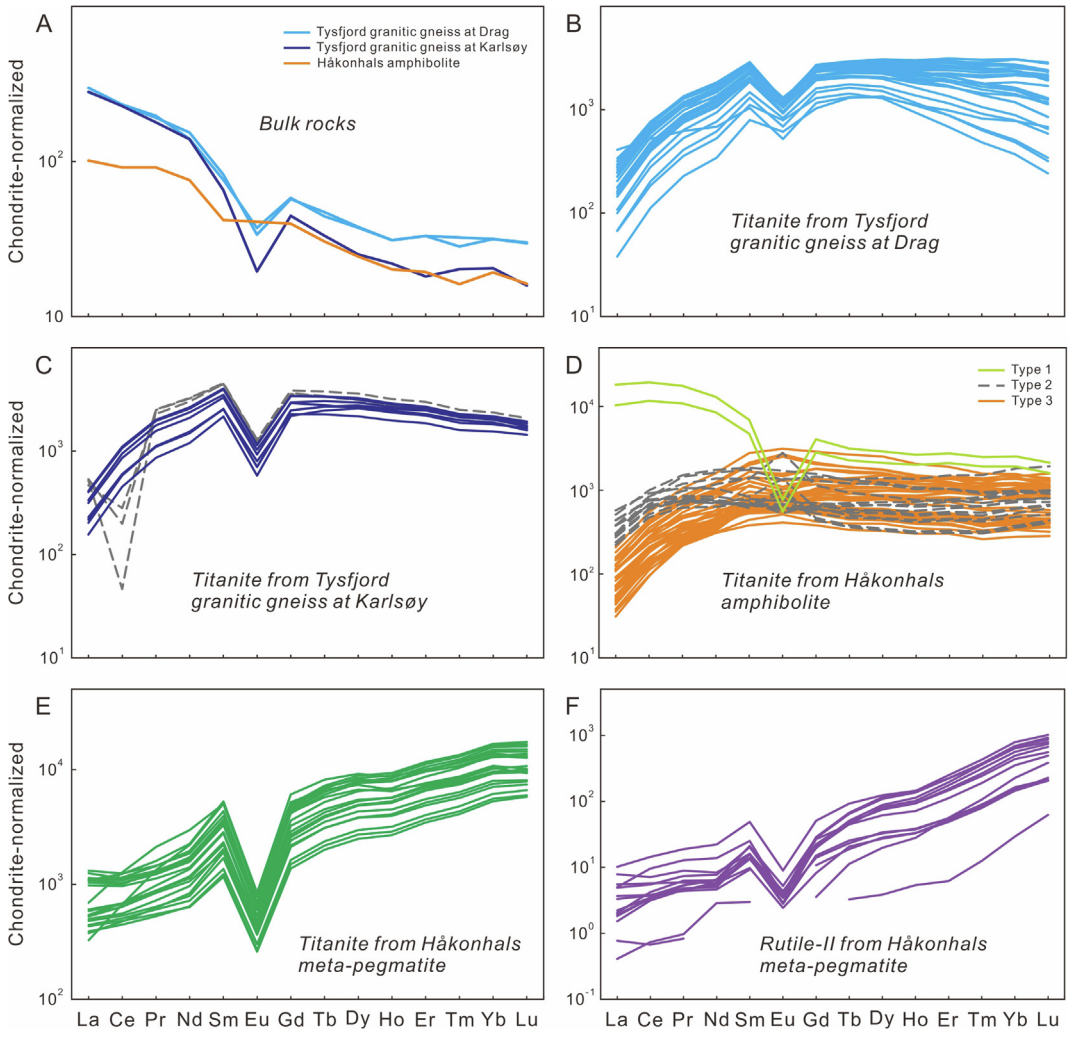

Fig. 11. Chondrite-normalized REE patterns of bulk rocks (A), titanite (B–E), and rutile-II (F). Chondrite data are from Barrat et al. (2012). The dash lines in C represent analyses showing negative Ce anomalies, which might result from local-scale processes (see supplementary text).

origin of these minerals. The high X_{An} plagioclase and high X_{Na} biotite, in equilibrium with titanite and hornblende (Fig. 6A–6D), are interpreted to be in the peak assemblage and might have been replaced to form the low X_{An} plagioclase and low X_{Na} biotite (together with Ba-rich K-feldspar) during retrogression. Quartz, zircon, and fluorapatite coexist with titanite and hornblende, indicating that some of them also crystallized at the peak stage. Therefore, we submit a peak assemblage of hornblende + high X_{An} plagioclase + high X_{Na} biotite + K-feldspar + quartz + titanite + epidote-group minerals + fluorapatite + zircon (+garnet at Drag) for the Caledonian metamorphism in the granitic gneiss. The Håkonhals amphibolite, showing similar mineral texture and sequences (Figs. 6E–6F and 7G–7I), is made up of the same peak assemblage (without K-feldspar) as the granitic gneiss. A mafic protolith (mega-enclave or intrusion) for the amphibolite is implied by its high TiO_2, MgO, FeO, low REE content and no Eu anomaly (Table S4; Fig. 11A).

The equilibrium texture between titanite, epidote-group minerals, quartz, and high X_{An} plagioclase in the granitic gneiss and the amphibolite (Figs. 6 and 7) indicates a TZARS equilibrium reaction of 2 zoisite/clinozoisite (Cz) + rutile (Rt) + quartz (Qz) = 3 anorthite (An) + titanite (Ttn) + H_2O (Frost et al., 2001). The TZARS barometer has proven to provide accurate pressure estimates for epidote-bearing amphibolite facies (Kapp et al., 2009). Following the protocol of Kapp et al. (2009), a_{Cz} and a_{An} were calculated via the program AX (a_i: the activity of component i; Holland, 2002) using the averages of measured mineral compositions, and a_{Ttn} was calculated based on an ideal mixing model $a_{Ttn} = X_{Ti}$. a_{Rt} was assumed to be 0.85 ± 0.10, an average value for most titanite-bearing, rutile-absent amphibolites (Kapp et al., 2009; Chambers and Kohn, 2012). a_{Qz} and a_{H2O} were both set at 1 unity given the coexisting quartz and abundant hydrous minerals. Pressures were calculated by the average pressure module of THERMOCALC (Powell et al., 1998).

Table 3 shows all calculated component activities and pressure results. The latter are consistent within errors for the Tysfjord granitic gneiss and the Håkonhals

Table 1
Sample information, results of thermo-barometers, and U-Pb ages for the (meta-)pegmatites and the host rocks in Tysfjord, Northern Norway.

Locality	Sample	Mineral assemblage[a]	Pressure (kbar, σ)	Temperature (°C, σ)				Chronometers and U-Pb ages (Ma, 2σ)	
			TZARS[b]	Ti-in-Ca amphibole	Hbl-Pl A[c]	Hbl-Pl B[d]	Zr-in-titanite	Magmatism	Metamorphism
Tysfjord granitic gneiss									
Jennyhaugen, Drag	2922	Hbl + Bt + Qz + Kfs + Pl + Ttn + Ep + Fap + Grt	12.7 ± 1.1	**709 ± 10 (n = 10)**	**701 ± 20 (n = 10)**	656 ± 11 (n = 10)	**742 ± 3 (n = 14)**	Zircon: 1801 ± 6[e]	Titanite: 410.6 ± 1.5
Nedre Øyvollen, Drag	0117	Hbl + Bt + Qz + Kfs + Pl + Ttn + Ep + Fap + Grt	12.5 ± 1.1	**709 ± 10 (n = 12)**	**707 ± 25 (n = 12)**	649 ± 15 (n = 12)	**748 ± 4 (n = 14)**		
Karlsøy	3122	Hbl + Bt + Qz + Kfs + Pl + Ttn + Ep + Fap	13.6 ± 1.3	625 ± 19 (n = 12)	**719 ± 37 (n = 12)**	644 ± 16 (n = 11)	**749 ± 4 (n = 11)**	Zircon: 1805 ± 1[e]	Titanite: 409.1 ± 3.4
Amphibolite									
Håkonhals	0206	Hbl + Bt + Qz + Pl + Ttn + Ep + Fap	**12.1 ± 0.9**	601 ± 11 (n = 11)	**680 ± 7 (n = 11)**	**694 ± 9 (n = 11)**	**732 ± 4 (n = 9)**	Titanite: 1736 ± 3	Titanite: 413 ± 11
Meta-pegmatites									
Håkonhals	070201	Kfs + Qz + Ab + Rt + Ttn					**730 ± 3 (n = 22)**		Titanite: 409 ± 18
Hundholmen								Columbite: 1756 ± 5[e]	Columbite: 404 ± 28[e]
Tiltvika								Columbite: 1772 ± 3[e]	Columbite: 437 ± 24[e]
Stetind									Zircon, allanite, fergusonite, and uraninite: 410–400[f]
Pegmatites									
Tennvatn								Columbite: 383 ± 3[e]	
Tjeldøya								Columbite: 397 ± 3[e] Zircon: 393 ± 1[e]	

[a] Abbreviations: Ab-albite, Bt-biotite, Ep-epidote-group minerals, Fap-fluorapatite, Grt-garnet, Hbl-hornblende, Kfs-K-feldspar, Pl-plagioclase, Qz-quartz, Rt-rutile, Ttn-titanite.
[b] TZARS barometer: 2 zoisite/clinozoisite + rutile + quartz = 3 anorthite + titanite + H_2O.
[c] Thermometer A: edenite + 4 quartz = tremolite + albite.
[d] Thermometer B: edenite + albite = richterite + anorthite.
Please note that for the pressures and temperatures, values in bold are recommended or meaningful (see text for explanation).
Data source: [e] Müller et al., 2022; [f] Hetherington et al., 2021; all titanite ages are from this study. Lower intercepts of the discordia columbite U-Pb ages are taken as metamorphic ages for the *meta*-pegmatites.

Table 2
TIMS U-Pb dates of titanite from the Tysfjord granitic gneiss and the Håkonhals amphibolite.

Sample	Titanite description	Composition		Radiogenic isotopic ratios								Isotopic ages (Ma)					
		Th/U	Pb_c (pg)[a]	$^{206}Pb/^{204}Pb$	$^{207}Pb/^{206}Pb$	2σ	$^{207}Pb/^{235}U$	2σ	$^{206}Pb/^{238}U$	2σ	rho[b]	$^{207}Pb/^{206}Pb$	2σ	$^{207}Pb/^{235}U$	2σ	$^{206}Pb/^{238}U$	2σ
Tysfjord granitic gneiss at Jennyhaugen, Drag																	
610/s1	Large light yellow grain, >200 μm	0.15	50	69	0.0552	0.0025	0.4995	0.0232	0.0656	0.0005	0.228	420	101	411.4	15.7	409.7	3.3
610/s2	Large light yellow grain, >200 μm	0.56	26	47	0.0495	0.0097	0.4493	0.0914	0.0658	0.0013	0.464	171	455	376.8	64.1	411.0	7.9
610/s3	Large light yellow grain, >200 μm	0.53	22	63	0.0552	0.0122	0.5050	0.1166	0.0663	0.0016	0.479	422	492	415.1	78.7	413.8	9.7
610/s13	Large light yellow grain, >200 μm	0.10	15	64	0.0494	0.0059	0.4378	0.0551	0.0643	0.0010	0.446	166	280	368.7	38.9	401.8	5.8
Tysfjord granitic gneiss at Karlsøy																	
610/s11	Large light yellow grain, >200 μm	0.16	69	68	0.0537	0.0047	0.4835	0.0444	0.0653	0.0008	0.379	360	198	400.5	30.4	407.6	4.7
610/s14	Large light yellow grain, >200 μm	0.34	60	58	0.0553	0.0033	0.4983	0.0310	0.0654	0.0007	0.240	424	135	410.6	21.0	408.3	4.1
610/s15	Large light yellow grain, >200 μm	0.58	27	53	0.0493	0.0066	0.4484	0.0629	0.0659	0.0010	0.432	164	314	376.2	44.1	411.6	6.1
610/s32	Large light yellow grain, >200 μm	0.51	22	63	0.0525	0.0113	0.4794	0.1075	0.0662	0.0015	0.486	309	488	397.6	73.8	413.0	9.0
Håkonhals amphibolite																	
611/s113	Large darker yellow grain[c]	0.58	9	1037	0.1044	0.0001	3.9222	0.0133	0.2725	0.0008	0.942	1703	1	1618.3	1.4	1553.6	2.0
611/s114	Large light yellow grain[c]	1.02	13	33	0.0684	0.0187	0.7235	0.2109	0.0767	0.0026	0.582	881	283	552.7	62.1	476.4	7.8
611/s115	Several smaller light yellow grains[c]	0.50	8	47	0.0577	0.0081	0.5493	0.0824	0.0691	0.0015	0.472	518	155	444.6	27.0	430.5	4.4

[a] Pb_c: total common Pb in sample (initial + blank).
[b] Rho: error correlations.
[c] Based on their colors, it is inferred that 611/s113 represents type 1 titanite, while 611/s114 and 611/s115 represent type 2 or 3 titanite.

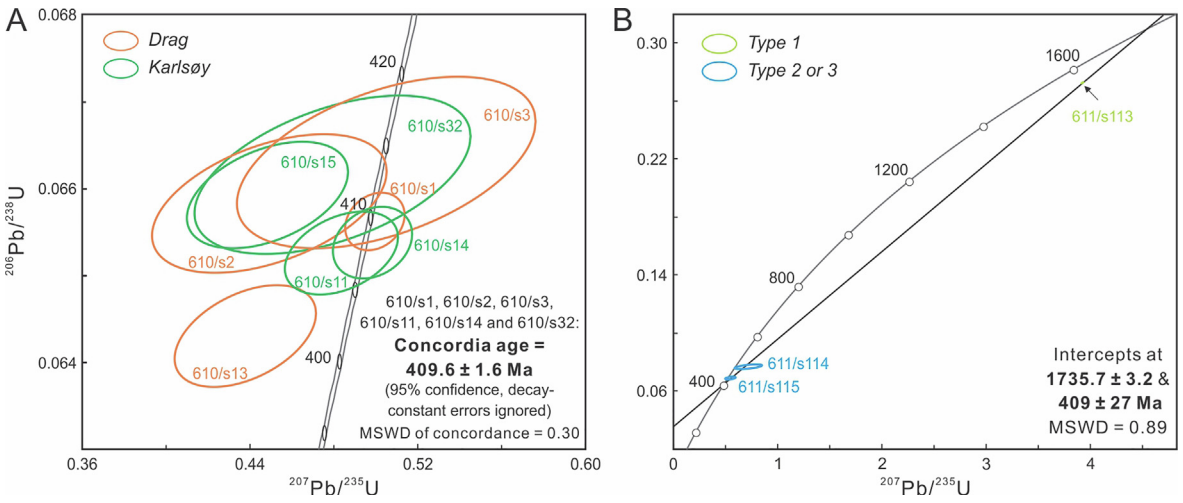

Fig. 12. Wetherill concordia diagrams for the TIMS U-Pb isotopic data of titanite from the Tysfjord granitic gneiss at Drag and Karlsøy (A) and the Håkonhals amphibolite (B). Data-point error ellipses are 2σ.

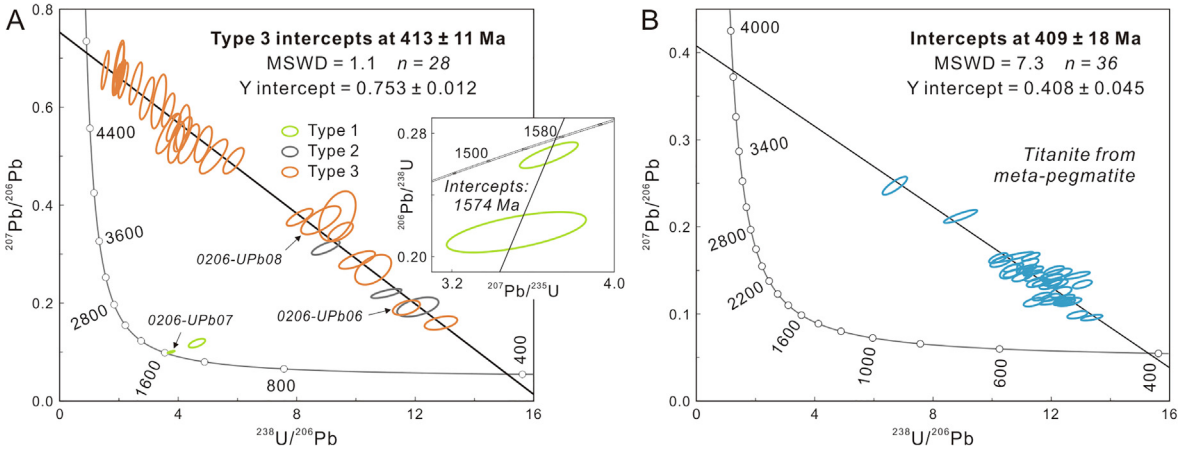

Fig. 13. Tera-Wasserburg diagrams for the LA-ICP-MS U-Pb isotopic data of titanite from the Håkonhals amphibolite (A) and the Håkonhals *meta*-pegmatite (B). Data-point error ellipses are 2σ. A Wetherill concordia diagram is embedded in A to show the data points of type 1 titanite. Locations of analyses 0206-UPb06 to -UPb08 are marked in Fig. 7H.

Table 3
Activities of components and calculated pressures from the TZARS barometry.

Sample	a_{Cz}	a_{TiO2}	a_{Qz}	a_{An}	a_{Ttn}	a_{H2O}	P (kbar)
2922	0.14 ± 0.02	0.85 ± 0.10	1	0.15 ± 0.02	0.80 ± 0.01	1	12.7 ± 1.1
0117	0.12 ± 0.02	0.85 ± 0.10	1	0.16 ± 0.02	0.78 ± 0.03	1	12.5 ± 1.1
3122	0.08 ± 0.01	0.85 ± 0.10	1	0.09 ± 0.01	0.83 ± 0.02	1	13.6 ± 1.3
0206	0.27 ± 0.02	0.85 ± 0.10	1	0.26 ± 0.02	0.91 ± 0.01	1	12.1 ± 0.9

TZARS: 2 zoisite/clinozoisite (Cz) + rutile (Rt) + quartz (Qz) = 3 anorthite (An) + titanite (Ttn) + H_2O.
a_i: activity of component *i*. All errors are within 1σ.

amphibolite. However, the TZARS barometry is mainly built up on mafic amphibolites (Kapp et al., 2009), and plagioclase with lower X_{An} and epidote-group minerals with high LREE contents could bring additional uncertainty in calculating a_{An} and a_{Cz} for the granitic gneiss. Hence, the value from the amphibolite, 12.1 ± 1.8 kbar (2σ), is taken as the best estimate of the peak pressure of the region.

Zirconium-in-titanite thermobarometry has been calibrated by Hayden et al. (2008) as:

$$T\ (\circ C) = [7708 + 96 \times P\ (kbar)] / [10.52 - \log (Zr\ ppm) - \log (a_{SiO2}) - \log (a_{TiO2})] - 273.$$

Although elevated Al content in titanite ($a_{Ttn} < 1$) may cause additional deviation for the calibration, it still works well for titanite of $X_{Ti} \geq 0.8$ (Tropper and Manning, 2008) which is the case for the Tysfjord titanite. The coexistence of zircon with titanite (Fig. 7A–7C and 7H) meets the prerequisite of $a_{zircon} = 1$ for the calibration. Likewise, a_{SiO2} and a_{TiO2} were set at 1 unity and 0.85 ± 0.10, respectively. Using the peak pressure derived from the TZARS barometry, estimated temperatures are 745 ± 4 °C (Drag) and 749 ± 8 °C (Karlsøy) for the granitic gneiss and 732 ± 8 °C for the amphibolite (Table 1; 2σ uncertainty of the average; errors of pressure, $a_{TiO2,}$ and Zr content were propagated into temperature calculation for each data point). These values (742 ± 8 °C, 2σ) are identical, interpreted as the peak temperatures for the region.

Holland and Blundy (1994) put forward the hornblende-plagioclase thermometer (Hbl-Pl; errors = ± 40 °C) that comprises two reactions over 400–900 °C: A) edenite + 4 quartz = tremolite + albite; and B) edenite + albite = rich terite + anorthite (Hbl-Pl B requires plagioclase with X_{An} = 10–90, not applicable for the granitic gneiss). We thus further calculated the peak temperatures using the compositions of the coexisting hornblende and high X_{An} plagioclase (Table 1). This yields peak temperatures of 704 ± 23 °C (1σ; Drag) and 719 ± 37 °C (Karlsøy) for the granitic gneiss (Hbl-Pl A) and 687 ± 10 °C for the amphibolite (average of Hbl-Pl A and B).

In addition, we test the temperatures via Ti-in-calcium amphibole thermometry calibrated as (1σ: ± 35 °C; apfu: atom per formula unit; Liao et al., 2021):

$$T(^{\circ}C) = 2400/[1.52 - \log (\text{total Ti in apfu})] - 273.$$

There are three prerequisites for applying this thermometer (Liao et al., 2021): 1) the presence of Ti-phases such as titanite (abundant in Tysfjord); 2) in sub-alkaline systems (not applicable to the amphibolite); and 3) oxygen fugacity (fO_2) below NNO + 2 (the presence of sulfides like pyrite and the lack of sulfates in Tysfjord suggest fO_2 < SSO; SSO ≈ NNO + 2 based on Mungall, 2002; NNO: Ni-NiO oxygen buffer, SSO: sulfide-sulfur oxide buffer). This thermometer, calibrated against experimental data for Ti in Ca-amphibole over the range of 0.1–0.5 apfu, is only applicable to the hornblende from the granitic gneiss at Drag (Fig. 8A), which yields temperatures of 709 ± 10 °C.

The results based on the Hbl-Pl and Ti-in-calcium amphibole thermometry, within the uncertainties of these two methods, are identical to the Zr-in-titanite temperatures, which verifies the robustness of our thermobarometric estimates. Therefore, based on the titanite-specific thermo-barometers, we submit the peak metamorphism of 12.1 ± 1.8 kbar and 742 ± 8 °C in Tysfjord, which represent the first robust estimate for the Caledonian metamorphism in the lower part of the nappe stack. The estimate is consistent with high-grade amphibolite to high-pressure granulite facies conditions.

To the northeast of the Tysfjord granitic gneiss (near Efjord), Hodges and Royden (1984) estimated peak conditions of 13–14 kbar and 750–800 °C by kyanite-garnet-relevant equilibrium reactions for the kyanite pelitic schist from the Narvik Nappe Complex in the upper part of the nappe stack (Fig. 1B). Similarly, Steltenpohl and Bartley (1987) observed a high metamorphic grade of 10.6 kbar and 690 °C for the metapelites in Skånland (Fig. 1B), but interpreted it as a pre-Silurian metamorphic event and proposed the Caledonian metamorphism at 9 kbar and 630 °C for the upper stack. Our estimate of the metamorphic conditions of the Tysfjord region is comparable to that of the upper nappe stack from Hodges and Royden (1984).

5.2. P-T constraints on the metamorphosed pegmatite

The rutile-titanite assemblage of the Håkonhals *meta*-pegmatite gives more straightforward insights into how the Caledonian metamorphism reworked the Paleoproterozoic pegmatites. Rutile-I, as the core of the assemblage, is characterized by high Nb_2O_5 content (16–21 wt%). Such high values have only been reported in pegmatitic rutile (e.g., 28 wt% for the McGuire granitic pegmatite in Colorado; Černý et al., 1999) but are never found in metamorphic rutile (e.g., 3–5 wt% for the Malene supracrustal gneisses in West Greenland; Dymek, 1983). We thus interpret rutile-I and its primary population 1 inclusions, polycrase-I, as Paleoproterozoic pegmatitic minerals. The group of rutile-II, titanite, quartz, and minor polycrase-II and columbite-(Fe), rimming rutile-I and being aligned along the foliation, represent products into which rutile-I and polycrase-I decomposed during the Caledonian metamorphism. This scenario is in line with the recrystallization of chemically 'dirty' rutile-I as purer rutile-II (Fig. 10A), which is capable of lowering the Gibbs free energy of crystals.

The high F and Al contents in the resultant titanite require Ca-, F-, and Al-bearing reactants. Possible reactants among typical NYF pegmatitic minerals include fluorite and feldspars, which happened to have been encapsulated as population 2 inclusions in rutile-I (Fig. 9C). This implies decomposition reactions simplified as: rutile-I (high Nb, Fe) + fluorite + feldspars + polycrase-I → rutile-II + titanite + columbite-(Fe) + polycrase-II. Excessive components such as Sn, W, and Zr released from rutile-I account for the products of minor cassiterite, scheelite, wolframite, and zircon. Hence, population 3 inclusions in rutile-I are very likely to result from shearing-induced exsolution or decomposition from rutile-I upon metamorphism (Fig. 9D), provided the preferential orientation of neoblasts along the less-strained conjugate joints.

The titanite is in equilibrium with zircon in the *meta*-pegmatite (Fig. 9F–9H). In the presence of quartz and rutile, both a_{SiO2} and a_{TiO2} were set as 1 unity for the Zr-in-titanite thermobarometry. The amphibolite is sitting on

the *meta*-pegmatite, whose metamorphic pressure can be regarded as the condition of the *meta*-pegmatite. We thus estimated temperatures of 730 ± 6 °C (2σ) for the *meta*-pegmatite. This is identical to the Zr-in-titanite temperatures of the amphibolite and only about 5–30 °C lower than that of the granitic gneiss, which might reflect slightly lower metamorphic temperatures for the *meta*-pegmatite or is more likely to result from the marginal inaccuracy of some parameters (e.g., pressure, a_{TiO2}).

Zirconium-in-rutile is also a widely used thermobarometer and relatively less sensitive to pressure, calibrated in the β-quartz field as (Tomkins et al., 2007):

$$T\,(^{\circ}C) = [85.7 + 0.473 \times P\,(kbar)] / [0.1453 - 0.0083144 \times \ln(Zr\ ppm)] - 273.$$

The Zr-in-rutile-II thermobarometry yields 551 ± 2 °C (2σ) at the peak pressure and ~515 °C at a pressure down to 4 kbar. Surprisingly, they are ~200 °C lower than the Zr-in-titanite temperature, although the intergrowth texture and comparable REE patterns of rutile-II and titanite suggest simultaneous crystallization (Figs. 9F, 11E, and 11F).

During retrogression from high-grade metamorphism, Zr in rutile can re-equilibrate by diffusion (e.g., Luvizotto and Zack, 2009). Below 770 °C, the relatively smaller activation energy for diffusion in rutile makes Zr diffuse much faster in rutile than in titanite, especially for small grain sizes and under slow cooling rates, so rutile is less retentive of Zr than titanite (Cherniak, 2006; Cherniak et al., 2007). In the *meta*-pegmatite, rutile-II is much smaller than titanite and is surrounded by later hydrous phases (e.g., chlorite; Fig. 9B), which implies the impact of hydrous retrogression. The region has slow cooling rates (see discussion below). Therefore, we argue that Zr in rutile-II is more likely to reflect intense diffusive re-equilibration. The irregular zonation in rutile-II (Fig. 9H and 9I) probably hints at such diffusive processes.

5.3. Titanite geochemistry fingerprinting metamorphic processes

This section aims to fingerprint metamorphic processes mainly in terms of REE geochemistry of titanite. Firstly, we clarify that the REE patterns of metamorphic titanite from the Tysfjord granitic gneiss are featured by depleted LREE and flat to fractionated HREE (Fig. 7B and 7C), which we attribute to the growth of epidote-group minerals (rich in LREE) and garnet (accounting for HREE fractionation in titanite at Drag), respectively. A detailed explanation of mineralogical controls on the REE patterns of titanite is provided in the supplementary text.

In the Håkonhals amphibolite there are three types of titanite, showing variations in U-Pb isotopic ratios and trace elements. Type 1 titanite is interpreted as inherited grains from the mafic protolith of the amphibolite, indicated by: 1) metamorphic epidote-group minerals present in type 3 rather than type 1 (Fig. 7H); 2) its optically darker yellow color and LREE-rich patterns different from the metamorphic titanite in the Tysfjord granitic gneiss (Fig. 11); 3) its extraordinary high Zr content indicating crystallization in zircon-free mafic rocks (no competition for Zr from zircon); and 4) its least-discordant U/Pb ages roughly defining a Paleoproterozoic crystallization age (Fig. 13A). By contrast, type 3 titanite, 1) of optically light yellow color, 2) having inherited cores of type 1 titanite (Fig. 7H), 3) showing LREE-depleted patterns like the metamorphic titanite in the granitic gneiss (Fig. 11), and 4) having a Caledonian crystallization age (Fig. 13A), is inferred to represent neoblastic growth or complete recrystallization of inherited titanite (type 1) during the metamorphism. Type 2 titanite, featured by an optically light yellow color, moderate contents in Zr, Y, Nb, ΣREE, Th, and U (Fig. 10C), relatively flat REE patterns (Fig. 11D), and U/Pb isotopic ratios falling along the Caledonian isochron defined by type 3 (Fig. 13A), is best explained as partial recrystallization of inherited titanite during the metamorphism.

Therefore, the changes of U-Pb isotopes and trace elements record a recrystallization process of titanite driven by the metamorphism in the amphibolite. This interpretation is in good agreement with a statistical study on REE geochemistry of titanite showing a decreasing trend in LREE contents from igneous to recrystallized, metamorphic titanite (Scibiorski and Cawood, 2022). It is also supported by the TIMS U-Pb isotopic data of titanite from the amphibolite in Fig. 12B, where the upper intercept of 1735.7 ± 3.2 Ma gives a better constraint on the crystallization age for type 1 titanite, and the lower intercept of 409 ± 27 Ma represents the Caledonian reworking (e.g., Pb remobilization in type 1 titanite and recrystallization as type 2 or 3 titanite).

In the Håkonhals *meta*-pegmatite, the Nb/Ta ratios of the titanite can further attest aforementioned element diffusion in rutile-II during metamorphic retrogression. Variations of Nb/Ta in metamorphic rutile can reflect Nb/Ta decoupling in metamorphic fluids (e.g., Pereira et al., 2019) or result from diffusive Nb/Ta fractionation (e.g., Marschall et al., 2013) as Nb diffuses faster than Ta by a factor of 6–28 in rutile (Dohmen et al., 2019). In contrast, variations of Nb/Ta in metamorphic titanite are mainly dependent on Nb/Tb decoupling in the fluids (e.g., Chen and Zheng, 2015), as diffusive Nb/Ta fractionation is negligible due to similar diffusivities of Nb and Ta in titanite (Cherniak, 2015). In the *meta*-pegmatite (Fig. 10B), the small variations in Nb/Ta of titanite argue for insignificant Nb/Tb decoupling in the metamorphic fluids where titanite and rutile-II grew. Therefore, the large Nb/Ta variations in rutile-II reflect diffusive Nb/Ta fractionation. This is also

supported by: 1) the coexistence of columbite-(Fe) (Fig. 9), indicating extremely high Nb availability in the fluids; and 2) an irrelevant relation between Nb/Ta ratio and Ta content in rutile-II, ruling out Ta availability-caused Nb/Ta fractionation in the fluids which should result in a strong inverse correlation of Nb/Ta vs. Ta in rutile (e.g., Chen and Zheng, 2015).

5.4. Titanite petrochronology for regional metamorphism

In this study, the titanite from the Tysfjord granitic gneiss has identical TIMS ages at Drag and Karlsøy, pointing to c. 410 Ma that represents the first report of the peak metamorphic age of the granitic gneiss. The Scandian orogeny resulted in high-grade metamorphism on the allochthons and the Baltic basement in the period of 440–400 Ma (up to eclogite-facies; Spengler et al., 2009; Corfu et al., 2014; Froitzheim et al., 2016; Warvik et al. 2022). Thus, the peak metamorphism in Tysfjord was linked to the late event of the ~40 Ma-lasting Scandian orogenic cycle.

The Tysfjord granitic gneiss is mainly overlain by the exotic Uppermost and Upper Allochthons (exotic in relation to Baltica; Gee and Sturt, 1985; Gee et al., 2008). The timing of the nappe stacking of these exotic allochthons onto the Baltic basement was diachronous along the strike of the orogeny (Warvik et al. 2022), but just to the south of the Tysfjord window, arc magmatism in the Beiarn nappe complex of the Uppermost Allochthon occurred at ~430 Ma (Augland et al., 2012b), thus indicating that nappe stacking onto Baltica in this part of the orogeny commenced after that time. Remarkably, zircon in the sheared granite in the Beiarn nappe complex yielded a recrystallization age of ~414 Ma (Augland et al., 2012b), which is indicative of the metamorphism and deformation of the Uppermost Allochthon. To the south of Tysfjord, metamorphic titanite and zircon were dated to 430–400 Ma for the Baltic basement in the Nasafjället window below the Upper Allochthon and the Sjona and Høgtuva windows below the Uppermost Allochthon (Fig. 1A; Essex and Gromet, 2000; Larsen et al., 2002; Schilling et al., 2015), taken as the minimum age of the nappe stacking of the exotic allochthons. Therefore, the metamorphism in the Tysfjord granitic gneiss was very likely caused by the nappe stacking of the exotic allochthons onto Baltica, and the titanite ages presented here most likely closely represent the timing of maximum burial.

To the east of Tysfjord, the Narvik nappe complex in the Upper Allochthon shows peak ages around 432 Ma (monazite and zircon U-Pb; Northrup, 1997), which are ~20 Ma older than the titanite ages for Tysfjord. However, a similar younger metamorphic age of ~415 Ma for fine-grained titanite was reported for the basal Uppermost Allochthons that is just above the Narvik nappe complex (Northrup, 1997). Without coupled information on P-T, we cannot infer that the older ages indicate earlier metamorphism owing to the nappe stacking of the Upper Allochthons. However, we can highlight the advantage of titanite in obtaining integrated P-T-t information.

5.5. Linking rare-element (meta-)pegmatites to Caledonian metamorphism

The titanite from the Håkonhals *meta*-pegmatite apparently yields an age of 409 ± 18 Ma and an initial $^{207}Pb/^{206}$-Pb ratio of 0.408 ± 0.045 (Fig. 13B), but the excess scatter of the U-Pb isotopic data clearly indicates mixing between several Pb-isotopic components. In conjunction with the reported protolith ages of ~1.8 Ga from the granitic gneiss and the regional *meta*-pegmatites (Table 1; Müller et al., 2022), and the Caledonian metamorphic age from the neighboring amphibolite (consistent lower intercept ages of 413 ± 11 Ma and 409 ± 27 Ma determined from the LA-ICP-MS and TIMS U-Pb data, respectively; Figs. 12B and 13A), a mixing scenario between a Paleoproterozoic magmatic component and the Caledonian metamorphic overprint best explains the observed U-Pb isotopic system in the titanite from the *meta*-pegmatite (see more discussions below), meaning that this titanite is compatible with a metamorphic crystallization equivalent to that of the granitic gneiss (~410 Ma). This, integrated with the parallel foliation and comparable P-T conditions between the *meta*-pegmatite and the granitic gneiss, confirms the same effects of the Caledonian metamorphism on the *meta*-pegmatite and the granitic gneiss.

Specifically, Pb compositions of the metamorphic titanite formed by Caledonian recrystallization of Paleoproterozoic precursors can be explained by mixing of three components: i) in-situ radiogenic Pb from Caledonian crystallization, ii) regional common Pb from surrounding rocks ($^{207}Pb/^{206}Pb$ = 0.863 at 410 Ma based on the evolution model of Stacey and Kramers, 1975), and iii) inherited Pb from precursors which is the mixing of iii-a) regional common Pb at the Paleoproterozoic crystallization and iii-b) radiogenic Pb from the Paleoproterozoic crystallization. The titanite from the *meta*-pegmatite shows an apparent initial $^{207}Pb/^{206}Pb$ ratio of 0.408 ± 0.045 lower than the regional common Pb component (ii), and the excessively scattered U/Pb isotopic ratios. This indicates a considerable inherited Pb component (iii) in the titanite from heterogeneous mixing of components iii-a) and -b). Such component (iii) is very likely from the breakdown of the polycrase-bearing rutile-I.

The robust regression of the U-Pb isotopic data of type 3 titanite in the amphibolite yields a resolvable initial $^{207}Pb/^{206}Pb$ ratio of 0.753 ± 0.012 (Fig. 13A), which is lower than the regional common Pb of 0.863 (Stacey and Kramers, 1975) or 0.821 ± 0.025 (determined from nominally U-free hornblende in the amphibolite; supplementary information). Likewise, an inherited Pb component (iii) in type 3 titanite is attested but is from relatively homogenous mixing of iii-a) and -b). It is probably from the U-rich precursor, type 1 titanite. This interpretation is also supported by the well-defined regression line and a comparable Caledonian lower intercept age for the TIMS data shown in Fig. 12B, where the common Pb components of all analyses are subtracted using the Stacey and Kramers (1975) Pb evolution model at 1.8 Ga. An inherited Pb component in the recrystallized titanite was also reported from the Caledo-

nian Western Gneiss Region, Norway (Gordon et al., 2021).

Hetherington et al. (2021) reported TIMS U-Pb ages of zircon, allanite, fergusonite, and uraninite in the range of 410–400 Ma for the Stetind "pegmatite" that should, as argued by Müller et al. (2022), belong to the *meta*-pegmatite suite based on its strong foliation and shearing characteristic. TIMS U-Pb dating on primary columbite from two *meta*-pegmatites in Tysfjord gave upper intercept ages in the Paleoproterozoic Svecofennian range but lower intercept ages of 404 ± 28 Ma and 437 ± 24 Ma, respectively (Table 1; Müller et al., 2022). These lower intercept ages and the ages for Stetind are, within errors, coeval with the regional metamorphism age of ~410 Ma, indicating the metamorphism on the Paleoproterozoic pegmatites has reset the U-Pb chronometers to various degrees.

Müller et al. (2022) reported the columbite and zircon U-Pb ages in the range of 400–380 Ma for two undeformed pegmatites in Tysfjord (Table 1), meaning that there was a lag of ~10–30 Ma between the formation of undeformed pegmatites and the peak metamorphism. Following the collisional Scandian orogeny, the post-collisional extension took place in the period of 400–380 Ma in the Central Scandinavian Caledonides, resulting from the reactivation of basal thrusts and formation of hinterland-dipping shear zones owing to the orogenic collapses (Gee et al., 2008; Steltenpohl et al., 2009; Fossen, 2010). The post-collisional extension is considered to form the culminations in the Baltic basement and exhume the high-grade complexes (Gee et al., 2008; Fossen, 2010)). During the top-W to NW extensional shearing and strike-slip (Gee et al, 2008), the Caledonian pegmatites in Tysfjord were probably formed by the B-rich fluid-driven anatexis of the granitic gneiss, given the high abundance of schorl in these pegmatites (Müller et al., 2022).

If we assume that the granitic gneiss was cooled down to ~600 °C at 380 Ma to be capable of generating anatectic melts (hydrous minimum melt temperatures; Simmons and Webber, 2008), the cooling rates should be no higher than 5 °C/Ma. Such persistently slow cooling rates could set the granitic gneiss from 750 °C at 410 Ma to 350 °C at 330 Ma. This rough estimation agrees with the biotite-whole rock Rb-Sr isochron ages of 347 ± 7 Ma for the granitic gneiss, taking Sr-closure temperature of 350 °C for biotite (Andresen and Tull, 1986). The granitic gneiss is relatively rich in radioactive elements, e.g., 56 ppm Th and 15 ppm U in the north (Romer et al., 1992; Müller, 2011). The radioactive decay perhaps brought up supplementary heat to slow down the cooling (Fossen et al., 2017). A slow cooling rate favors the Zr diffusion in rutile-II from the *meta*-pegmatite. Interestingly, the closure temperature for Zr diffusion in rutile of 30–80 μm grain radius (30 μm is the minimum analyzable size by laser in this study) is experimentally shown to be ~520–550 °C at cooling rates of 1–10 °C/Ma and fO_2 of the FMQ buffer (fayalite-magnetite-quartz; Dohmen et al., 2019), which is concordant with the temperature estimates from Zr in rutile-II.

6. CONCLUSIONS

The TZARS barometry, Zr-in-titanite thermobarometry, and titanite U-Pb chronology yield the peak Caledonian metamorphism of 12.1 ± 1.8 kbar, 730–750 °C, and ~410 Ma for the largest *meta*-pegmatite and the host rocks in Tysfjord. Comparable P-T-t history of the *meta*-pegmatite to the regional metamorphism, integrated with previous dating results for the regional *meta*-pegmatites (interpreted as Caledonian reworking here), indicates that the Paleoproterozoic pegmatites underwent the same metamorphism as the region caused by the nappe stacking at the late Scandian orogeny. Our results also support the genetic linkage of young pegmatites to the Caledonian post-collisional extension and imply a slow cooling history for the region.

This study illustrates the merits of titanite geochemistry in understanding the metamorphic evolution of *meta*-pegmatites in orogenic belts. The Caledonian orogeny caused strong shearing and deformation of pegmatitic bodies, breakdown of pegmatitic U-Pb geochronometers (e.g., Nb-rutile → rutile + titanite), and further reworked their U-Pb isotopic systems and trace element geochemistry (e.g., inherited Pb components in titanite, Zr-re-equilibration and diffusive Nb/Ta fractionation in rutile). The observed variations of trace elements and U-Pb isotopic systems in titanite record the metamorphism-driven recrystallization of inherited titanite, which exemplifies combined texture, trace elements, and U-Pb isotopic ratios of titanite in provenance discrimination. Our study cautions against interpreting tectonomagmatic events by *meta*-pegmatite-derived ages without textural and geochemical examination.

DECLARATION OF COMPETING INTEREST

The authors declare that they have no known competing financial interests or personal relationships that could have appeared to influence the work reported in this paper.

ACKNOWLEDGMENTS

This study was funded by European Commission's Horizon 2020 innovation program under grant agreement No 869274, project GREENPEG New Exploration Tools for European Pegmatite Green-Tech Resources. Tomas Husdal is thanked for his support during the fieldwork at Håkonhals and a thorough review of an early version of this manuscript. We are grateful to Gunborg Bye Fjeld for the help in titanite separation, Jesse Walters for the directions in using the TZARS barometry, and Henrik Friis, Tom Andersen, and William Keyser for the discussion. We are also thankful to Craig Storey and two anonymous reviewers for their constructive comments and Associate Editor Tsuyoshi Iizuka for handling the manuscript.

APPENDIX A. SUPPLEMENTARY MATERIAL

Supplementary material to this article can be found online at https://doi.org/10.1016/j.gca.2022.06.014.

REFERENCES

Andresen A. and Tull J. F. (1986) Age and tectonic setting of the Tysfjord gneiss granite, Efjord, North Norway. *Nor. Geol. Tidsskr.* **66**, 69–80.

Andersen T., Andersson U. B., Graham S., Åberg G. and Simonsen S. L. (2009) Granitic magmatism by melting of juvenile continental crust: new constraints on the source of Palaeoproterozoic granitoids in Fennoscandia from Hf isotopes in zircon. *Journal of the Geological Society* **166**, 233–247.

Augland L. E., Andresen A. and Corfu F. (2010) Age, structural setting, and exhumation of the Liverpool Land eclogite terrane, East Greenland Caledonides. *Lithosphere* **2**, 267–286.

Augland L. E., Andresen A., Corfu F. and Daviknes H. K. (2012a) Late Ordovician to Silurian ensialic magmatism in Liverpool Land, East Greenland: new evidence extending the northeastern branch of the continental Laurentian magmatic arc. *Geol. Mag.* **149**, 561–577.

Augland L. E., Andresen A., Corfu F., Simonsen S. L. and Andersen T. (2012b) The Beiarn Nappe Complex: A record of Laurentian Early Silurian arc magmatism in the Uppermost Allochthon, Scandinavian Caledonides. *Lithos* **146–147**, 233–252.

Ballo E. G., Augland L. E., Hammer Ø. and Svensen H. H. (2019) A new age model for the Ordovician (Sandbian) K-bentonites in Oslo, Norway. *Palaeogeogr. Palaeoclimatol. Palaeoecol.* **520**, 203–213.

Barnes C. G., Frost C. D., Yoshinobu A. S., McArthur K., Barnes M. A., Allen C. M., Nordgulen Ø. and Prestvik T. (2007) Timing of sedimentation, metamorphism, and plutonism in the Helgeland Nappe Complex, north-central Norwegian Caledonides. *Geosphere* **3**, 683–703.

Barrat J. A., Zanda B., Moynier F., Bollinger C., Liorzou C. and Bayon G. (2012) Geochemistry of CI chondrites: Major and trace elements, and Cu and Zn Isotopes. *Geochim. Cosmochim. Acta* **83**, 79–92.

Bartley J. M. (1982) Limited basement involvement in Caledonian deformation, Hinnøy, north Norway, and tectonic implications. *Tectonophysics* **83**, 185–203.

Bergh S. G., Kullerud K., Myhre P. I., Corfu F., Armitage P. E. B., Zwaan K. B. and Ravna E. J. K. (2014) Archaean elements of the basement outliers west of the Scandinavian Caledonides in Northern Norway: Architecture, evolution and possible correlation with Fennoscandia. In *Evolution of Archean Crust and Early Life* (eds. Y. Dilek and H. Furnes). Springer, Netherlands, Dordrecht, pp. 103–126.

Bowring J. F., McLean N. M. and Bowring S. A. (2011) Engineering cyber infrastructure for U-Pb geochronology: Tripoli and U-Pb_Redux. *Geochem. Geophys. Geosyst.* **12**, Q0AA19.

Buick I. S., Storkey A. and William I. S. (2008) Timing relationships between pegmatite emplacement, metamorphism and deformation during the intra-plate Alice Springs Orogeny, central Australia. *J. Metamorph. Geol.* **26**, 915–936.

Černý P. (1991a) Rare-element granitic pegmatites. Part I: Anatomy and internal evolution of pegmatite deposits. *Geosci. Can.* **18**, 49–67.

Černý P. (1991b) Rare-element granitic pegmatites. Part II: Regional to global environments and petrogenesis. *Geosci. Can.* **18**, 68–81.

Černý P. (1991c) Fertile granites of Precambrian rare-element pegmatite fields: is geochemistry controlled by tectonic setting or source lithologies? *Precambr. Res.* **51**, 429–468.

Černý P., Chapman R., Simmons W. B. and Chackowsky L. E. (1999) Niobian rutile from the McGuire granitic pegmatite, Park County, Colorado: Solid solution, exsolution, and oxidation. *Am. Mineral.* **84**, 754–763.

Černý P. and Ercit T. S. (2005) The classification of granitic pegmatites revisited. *The Canadian Mineralogist* **43**, 2005–2026.

Černý P., Novák M. and Chapman R. (1992) Effects of sillimanite-grade metamorphism and shearing on Nb-Ta oxide minerals in granitic pegmatites, Marsikov, northern Moravia, Czechoslovakia. *Can. Mineral.* **30**, 699–718.

Chambers J. A. and Kohn M. J. (2012) Titanium in muscovite, biotite, and hornblende: Modeling, thermometry, and rutile activities of metapelites and amphibolites. *Am. Mineral.* **97**, 543–555.

Chen Y. X. and Zheng Y. F. (2015) Extreme Nb/Ta fractionation in metamorphic titanite from ultrahigh-pressure metagranite. *Geochim. Cosmochim. Acta* **150**, 53–73.

Cherniak D. J. (2006) Zr diffusion in titanite. *Contrib. Miner. Petrol.* **152**, 639–647.

Cherniak D. J. (2015) Nb and Ta diffusion in titanite. *Chem. Geol.* **413**, 44–50.

Cherniak D. J., Manchester J. and Watson E. B. (2007) Zr and Hf diffusion in rutile. *Earth Planet. Sci. Lett.* **261**, 267–279.

Corfu F. (2004) U-Pb Age, setting and tectonic significance of the anorthosite–mangerite–charnockite–granite suite, Lofoten-Vesterålen, Norway. *J. Petrol.* **45**, 1799–1819.

Corfu F., Andersen T. and Gasser D. (2014) The Scandinavian Caledonides: main features, conceptual advances and critical questions. *Geol. Soc., London, Special Publ.* **390**, 9–43.

Dohmen R., Marschall H. R., Ludwig T. and Polednia J. (2019) Diffusion of Zr, Hf, Nb and Ta in rutile: effects of temperature, oxygen fugacity, and doping level, and relation to rutile point defect chemistry. *Phys. Chem. Miner.* **46**, 311–332.

Dymek R. F. (1983) Fe-Ti oxides in the Malene supracrustals and the occurrence of Nb-rich rutile. *Rapp. Grønl. Geol. Unders.* **112**, 83–94.

Eberlei T., Habler G., Grasemann B. and Abart R. (2014) Upper–greenschist facies intragrain deformation of albite in mylonitic meta–pegmatite and the influence of crystallographic anisotropy on microstructure formation. *J. Struct. Geol.* **69**, 47–58.

Elburg M. A., Bons P. D., Foden J. and Brugger J. (2003) A newly defined Late Ordovician magmatic-thermal event in the Mt Painter Province, northern Flinders Ranges, South Australia. *Aust. J. Earth Sci.* **50**, 611–631.

Essex R. M. and Gromet L. P. (2000) U-Pb dating of prograde and retrograde titanite growth during the Scandian orogeny. *Geology* **28**, 419–422.

Fossen H. (2010) Extensional tectonics in the North Atlantic Caledonides: a regional view. *Geol. Soc., London, Special Publ.* **335**, 767–793.

Fossen H., Cavalcante G. C. and de Almeida R. P. (2017) Hot Versus Cold Orogenic Behavior: Comparing the Araçuaí-West Congo and the Caledonian Orogens. *Tectonics* **36**, 2159–2178.

Franz G. and Morteani G. (1984) The formation of chrysoberyl in metamorphosed pegmatites. *J. Petrol.* **25**, 27–52.

Froitzheim N., Miladinova I., Janák M., Kullerud K., Ravna E. K., Majka J., Fonseca R. O. C., Münker C. and Nagel T. J. (2016) Devonian subduction and syncollisional exhumation of continental crust in Lofoten, Norway. *Geology* **44**, 223–226.

Frost B. R., Chamberlain K. R. and Schumacher J. C. (2001) Sphene (titanite): phase relations and role as a geochronometer. *Chem. Geol.* **172**, 131–148.

Garber J., Hacker B., Kylander-Clark A., Stearns M. and Seward G. (2017) Controls on trace element uptake in metamorphic titanite: Implications for petrochronology. *J. Petrol.* **58**, 1031–1057.

Gee D. G., Fossen H., Henriksen N. and Higgins A. K. (2008) From the early Paleozoic platforms of Baltica and Laurentia to

the Caledonide Orogen of Scandinavia and Greenland. *Episodes* **31**, 44–51.

Gee D. G., Juhlin C., Pascal C. and Robinson P. (2010) Collisional Orogeny in the Scandinavian Caledonides (COSC). *GFF* **132**, 29–44.

Gee D. G. and Stephens M. B. (2020) Chapter 20 Lower thrust sheets in the Caledonide orogen, Sweden: Cryogenian–Silurian sedimentary successions and underlying, imbricated, crystalline basement. *Geol. Soc., London, Memoirs* **50**, 495–515.

Gee D. G. and Sturt B. (1985) *The Caledonide Orogen-Scandinavia and Related Areas*. John Wiley and Sons, Chichester, p. 1266.

Glodny J., Grauert B., Fiala J., Vejnar Z. and Krohe A. (1998) Metapegmatites in the western Bohemian massif: ages of crystallisation and metamorphic overprint, as constrained by U-Pb zircon, monazite, garnet, columbite and Rb–Sr muscovite data. *Geol. Rundsch.* **87**, 124–134.

Glover A. S., Rogers W. Z. and Barton J. E. (2012) Granitic pegmatites: storehouses of industrial minerals. *Elements* **8**, 269–273.

Gordon S. M., Kirkland C. L., Reddy S. M., Blatchford H. J., Whitney D. L., Teyssier C., Evans N. J. and McDonald B. J. (2021) Deformation-enhanced recrystallization of titanite drives decoupling between U-Pb and trace elements. *Earth Planet. Sci. Lett.* **560**, 116810.

Grimmer J. C., Glodny J., Drüppel K., Greiling R. O. and Kontny A. (2015) Early- to mid-Silurian extrusion wedge tectonics in the central Scandinavian Caledonides. *Geology* **43**, 347–350.

Gysi A. P. and Williams-Jones A. E. (2013) Hydrothermal mobilization of pegmatite-hosted REE and Zr at Strange Lake, Canada: A reaction path model. *Geochim. Cosmochim. Acta* **122**, 324–352.

Habler G., Thöni M. and Miller C. (2007) Major and trace element chemistry and Sm–Nd age correlation of magmatic pegmatite garnet overprinted by eclogite-facies metamorphism. *Chem. Geol.* **241**, 4–22.

Haus R., Prinz S. and Priess C. (2012) Assessment of high purity quartz resources. In *Quartz: deposits, mineralogy and analytics* (eds. J. Götze and R. Möckel). Springer, Berlin, Heidelberg, pp. 29–51.

Hayden L. A., Watson E. B. and Wark D. A. (2008) A thermobarometer for sphene (titanite). *Contrib. Miner. Petrol.* **155**, 529–540.

Hetherington C. J., Mailloux G. A. and Miller B. V. (2021) A multi-mineral U-(Th)-Pb dating study of the Stetind pegmatite of the Tysfjord region, Norway, and implications for production of NYF-rare element pegmatites during orogenic collapse. *Lithos* **398–399**, 106257.

Hodges K. V. and Royden L. (1984) Geologic thermobarometry of retrograded metamorphic rocks: An indication of the uplift trajectory of a portion of the northern Scandinavian caledonides. *J. Geophys. Res. Solid Earth* **89**, 7077–7090.

Högdahl K., Andersson U. B. and Eklund O. (2004) The Transscandinavian Igneous Belt (TIB) in Sweden: a review of its character and evolution. *Geol. Surv. Finland Spec. Pap.* **37**, 125.

Holland, T. (2002) AX: A program to calculate activities of mineral endmembers from chemical analyses. http://ccp14.cryst.bbk.ac.uk/ccp/web-mirrors/crush/astaff/holland/index.html.

Holland T. and Blundy J. (1994) Non-ideal interactions in calcic amphiboles and their bearing on amphibole-plagioclase thermometry. *Contrib. Miner. Petrol.* **116**, 433–447.

Hossack J. R. and Cooper M. A. (1986) Collision tectonics in the Scandinavian Caledonides. *Geol. Soc., London, Special Publ.* **19**, 285–304.

Husdal T. (2008) The minerals of the pegmatites within the Tysfjord granite, northern Norway. *Norsk Bergverksmuseum Skrift* **38**, 5–28.

Jaffey A. H., Flynn K. F., Glendenin L. E., Bentley W. C. and Essling A. M. (1971) Precision measurement of half-lives and specific activities of ^{235}U and ^{238}U. *Phys. Rev. C* **4**, 1889–1906.

Kaeter D., Barros R. and Menuge J. F. (2021) Metasomatic high field strength element, tin, and base metal enrichment processes in lithium pegmatites from Southeast Ireland. *Econ. Geol.* **116**, 169–198.

Kaeter D., Barros R., Menuge J. F. and Chew D. M. (2018) The magmatic–hydrothermal transition in rare-element pegmatites from southeast Ireland: LA-ICP-MS chemical mapping of muscovite and columbite–tantalite. *Geochim. Cosmochim. Acta* **240**, 98–130.

Kapp P., Manning C. and Tropper P. (2009) Phase-equilibrium constraints on titanite and rutile activities in mafic epidote amphibolites and geobarometry using titanite–rutile equilibria. *J. Metamorph. Geol.* **27**, 509–521.

Karlsen T. A. (2000) Economic potential of potassic feldspar-rich gneisses in Tysfjord/Hamaroy, northern Norway. *Norges Geologiske Undersokelse Bulletin* **436**, 129–135.

Kennedy A. K., Kamo S. L., Nasdala L. and Timms N. E. (2010) Grenville skarn titanite: Potential reference material for SIMS U-Th–Pb analysis. *Can. Mineral.* **48**, 1423–1443.

Kesler S. E., Gruber P. W., Medina P. A., Keoleian G. A., Everson M. P. and Wallington T. J. (2012) Global lithium resources: Relative importance of pegmatite, brine and other deposits. *Ore Geol. Rev.* **48**, 55–69.

Kohn M. J. (2017) Titanite petrochronology. *Rev. Mineral. Geochem.* **83**, 419–441.

Kohn M. J. and Corrie S. L. (2011) Preserved Zr-temperatures and U-Pb ages in high-grade metamorphic titanite: evidence for a static hot channel in the Himalayan orogen. *Earth Planet. Sci. Lett.* **311**, 136–143.

Krogh T. E. (1982) Improved accuracy of U-Pb zircon ages by the creation of more concordant systems using an air abrasion technique. *Geochim. Cosmochim. Acta* **46**, 637–649.

Larsen Ø., Skår Ø. and Pedersen R.-B. (2002) U-Pb zircon and titanite geochronological constraints on the late/post-Caledonian evolution of the Scandinavian Caledonides in north-central Norway. *Nor. Geol. Tidsskr.* **82**, 1–13.

Liao Y., Wei C. and Rehman H. U. (2021) Titanium in calcium amphibole: Behavior and thermometry. *Am. Mineral.* **106**, 180–191.

Linnen R. L., Van Lichtervelde M. and Černý P. (2012) Granitic pegmatites as sources of strategic metals. *Elements* **8**, 275–280.

London D. (2008) Pegmatites. *Can. Mineral. Special Publ.* **10**, 368.

London D. and Kontak D. J. (2012) Granitic pegmatites: scientific wonders and economic bonanzas. *Elements* **8**, 257–261.

Ludwig K. R. (2003) *ISOPLOT 3.00: A Geochronological Toolkit for Microsoft Excel*. Berkeley Geochronology Center, California, Berkeley.

Lupulescu M. V., Chiarenzelli J. R., Pullen A. T. and Price J. D. (2011) Using pegmatite geochronology to constrain temporal events in the Adirondack Mountains. *Geosphere* **7**, 23–39.

Luvizotto G. L. and Zack T. (2009) Nb and Zr behavior in rutile during high-grade metamorphism and retrogression: An example from the Ivrea-Verbano Zone. *Chem. Geol.* **261**, 303–317.

Marschall H. R., Dohmen R. and Ludwig T. (2013) Diffusion-induced fractionation of niobium and tantalum during continental crust formation. *Earth Planet. Sci. Lett.* **375**, 361–371.

Martin R. F. and De Vito C. (2005) The patterns of enrichment in felsic pegmatites ultimately depend on tectonic setting. *Can. Mineral.* **43**, 2027–2048.

Müller, A. (2011) Potential of rare earth element and Zr-, Be, U-, Th-, (W-) mineralisations in central and northern Nordland - Part 2, Norges geologiske undersøkelse rapport, pp. 56.

Müller A., Ihlen P. M., Snook B., Larsen R. B., Flem B., Bingen B. and Williamson B. J. (2015) The chemistry of quartz in granitic pegmatites of southern Norway: Petrogenetic and economic implications. *Econ. Geol.* **110**, 1737–1757.

Müller A., Romer R. L. and Pedersen R.-B. (2017) The Sveconorwegian pegmatite province–thousands of pegmatites without parental granites. *Can. Mineral.* **55**, 283–315.

Müller A., Romer R. L., Augland L. E., Zhou H., Rosing-Schow N., Spratt J. and Husdal T. (2022) Two-stage regional rare-element pegmatite formation at Tysfjord, Norway: Implications for the timing of late Svecofennian and late Caledonian high-temperature events. *Int. J. Earth Sci.* **111**, 987–1007.

Müller A., Wanvik J. E. and Ihlen P. M. (2012) Petrological and chemical characterisation of high-purity quartz deposits with examples from Norway. In *Quartz: deposits, mineralogy and analytics* (eds. J. Götze and R. Möckel). Springer, Berlin, Heidelberg, pp. 71–118.

Mungall J. E. (2002) Roasting the mantle: Slab melting and the genesis of major Au and Au-rich Cu deposits. *Geology* **30**, 915–918.

Northrup C. J. (1997) Timing of Structural Assembly, Metamorphism, and Cooling of Caledonian Nappes in the Ofoten-Efjorden Area, North Norway: Tectonic Insights from U-Pb and $^{40}Ar/^{39}Ar$ Geochronology. *J. Geol.* **105**, 565–582.

Pedersen R. B., Bruton D. L. and Furnes H. (1992) Ordovician faunas, island arcs and ophiolites in the Scandinavian Caledonides. *Terra Nova* **4**, 217–222.

Pereira I., Storey C., Darling J., Lana C. and Alkmim A. R. (2019) Two billion years of evolution enclosed in hydrothermal rutile: Recycling of the São Francisco Craton Crust and constraints on gold remobilisation processes. *Gondwana Res.* **68**, 69–92.

Petrík I., Broska I., Lipka J. and Siman P. (1995) Granitoid allanite-(Ce): substitiution relations, redox conditions and REE distributions (on an example of I-type granitoids, western Carpathians, Slovakia). *Geol. Carpath.* **46**, 79–94.

Piber A., Tropper P. and Mirwald P. W. (2009) Geothermobarometry of a stilpnomelane–garnet-bearing metapegmatite: P-T constraints on the Eo-Alpine metamorphic overprint of the Austroalpine nappes north of the Tauern Window. *Mineral. Petrol.* **96**, 99–111.

Pouchou J.-L. and Pichoir F. (1991) Quantitative analysis of homogeneous or stratified microvolumes applying the model "PAP". In *Electron Probe Quantitation* (eds. K. F. J. Heinrich and D. E. Newbury). Springer, US, Boston, MA, pp. 31–75.

Powell R., Holland T. and Worley B. (1998) Calculating phase diagrams involving solid solutions via non-linear equations, with examples using THERMOCALC. *J. Metamorph. Geol.* **16**, 577–588.

Romer, R., Kjøsnes, B., Korneliussen, A., Lindahl, I., Skyseth, T., Stendal, M. and Sundvoll, B. (1992) The Archaean–Proterozoic boundary beneath the Caledonides of northern Norway and Sweden: U–Pb, Rb–Sr and Nd isotopic data from the Rombak–Tysfjord area, Norges geologiske undersøkelse rapport, pp. 67.

Schilling J., Bingen B., Skår Ø., Wenzel T. and Markl G. (2015) Formation and evolution of the Høgtuva beryllium deposit, Norway. *Contrib. Mineral. Petrol.* **170**, 30.

Schmitz M. D. and Schoene B. (2007) Derivation of isotope ratios, errors, and error correlations for U-Pb geochronology using ^{205}Pb-^{235}U-(^{233}U)-spiked isotope dilution thermal ionization mass spectrometric data. *Geochem. Geophys. Geosyst.* **8**, Q08006.

Scibiorski E. A. and Cawood P. A. (2022) Titanite as a petrogenetic indicator. *Terra Nova* **34**, 177–183.

Scibiorski E., Kirkland C., Kemp A., Tohver E. and Evans N. (2019) Trace elements in titanite: A potential tool to constrain polygenetic growth processes and timing. *Chem. Geol.* **509**, 1–19.

Simmons W., Falster A., Webber K., Roda-Robles E., Boudreaux A. P., Grassi L. R. and Freeman G. (2016) Bulk composition of Mt. Mica pegmatite, Maine, USA: implications for the origin of an LCT type pegmatite by anatexis. *Can. Mineral.* **54**, 1053–1070.

Simmons W. B. S. and Webber K. L. (2008) Pegmatite genesis: state of the art. *Eur. J. Mineral.* **20**, 421–438.

Soret M., Larson K. P., Cottle J. and Ali A. (2021) How Himalayan collision stems from subduction. *Geology* **49**, 894–898.

Spengler D., Brueckner H. K., van Roermund H. L. M., Drury M. R. and Mason P. R. D. (2009) Long-lived, cold burial of Baltica to 200 km depth. *Earth Planet. Sci. Lett.* **281**, 27–35.

Stacey J. S. and Kramers J. D. (1975) Approximation of terrestrial lead isotope evolution by a two-stage model. *Earth Planet. Sci. Lett.* **26**, 207–221.

Steltenpohl M. G. and Bartley J. M. (1987) Thermobarometric profile through the Caledonian nappe stack of Western Ofoten, North Norway. *Contrib. Miner. Petrol.* **96**, 93–103.

Steltenpohl M. G., Carter B. T., Andresen A. and Zeltner D. L. (2009) $^{40}Ar/^{39}Ar$ Thermochronology of Late- and Postorogenic Extension in the Caledonides of North-Central Norway. *J. Geol.* **117**, 399–414.

Storey C. D., Smith M. P. and Jeffries T. E. (2007) In situ LA-ICP-MS U-Pb dating of metavolcanics of Norrbotten, Sweden: Records of extended geological histories in complex titanite grains. *Chem. Geol.* **240**, 163–181.

Thöni M. and Miller C. (2004) Ordovician meta-pegmatite garnet (NW Ötztal basement, Tyrol, Eastern Alps): preservation of magmatic garnet chemistry and Sm–Nd age during mylonitization. *Chem. Geol.* **209**, 1–26.

Tomkins H. S., Powell R. and Ellis D. J. (2007) The pressure dependence of the zirconium-in-rutile thermometer. *J. Metamorph. Geol.* **25**, 703–713.

Tropper P. and Manning C. E. (2008) The current status of titanite–rutile thermobarometry in ultrahigh-pressure metamorphic rocks: The influence of titanite activity models on phase equilibrium calculations. *Chem. Geol.* **254**, 123–132.

Walters J. B. and Kohn M. J. (2017) Protracted thrusting followed by late rapid cooling of the Greater Himalayan Sequence, Annapurna Himalaya, Central Nepal: Insights from titanite petrochronology. *J. Metamorph. Geol.* **35**, 897–917.

Warvik K., Ringstad H. B., Augland L. E., Corfu F. and Gabrielsen R. H. (2022) The Revsegg and Kvitenut allochthons, Scandinavian Caledonides: origins and evolutions in the Caledonian Wilson cycle. *J. Geol. Soc.*, 179, jgs2021-062.

Zhang L., Chu X., Zhang L., Fu B., Bader T., Du J. and Li X. (2018) The early exhumation history of the Western Tianshan UHP metamorphic belt, China: new constraints from titanite U-Pb geochronology and thermobarometry. *J. Metamorph. Geol.* **36**, 631–651.

Associate editor: Tsuyoshi Iizuka